May 1980

Laser System for the Detection of Flaws
in Solids

by Ronald J. Wellman

U.S. Army Electronics Research
and Development Command

Harry Diamond Laboratories

Adelphi, MD 20783

Approved for public release; distribution unlimited.

REPORT DOCUMENTATION PAGE		READ INSTRUCTIONS BEFORE COMPLETING FORM
1. REPORT NUMBER HDL-TR-1902	2. GOVT ACCESSION NO.	3. RECIPIENT'S CATALOG NUMBER
4. TITLE *(and Subtitle)* Laser System for the Detection of Flaws in Solids		5. TYPE OF REPORT & PERIOD COVERED Technical Report
		6. PERFORMING ORG. REPORT NUMBER
7. AUTHOR(s) Ronald J. Wellman		8. CONTRACT OR GRANT NUMBER(s) DA: 1L161101A91A
9. PERFORMING ORGANIZATION NAME AND ADDRESS Harry Diamond Laboratories 2800 Powder Mill Road Adelphi, MD 20783		10. PROGRAM ELEMENT, PROJECT, TASK AREA & WORK UNIT NUMBERS Program Ele: 61101A
11. CONTROLLING OFFICE NAME AND ADDRESS U.S. Army Materiel Development and Readiness Command Alexandria, VA 22333		12. REPORT DATE May 1980
		13. NUMBER OF PAGES 33
14. MONITORING AGENCY NAME & ADDRESS*(If different from Controlling Office)*		15. SECURITY CLASS. *(of this report)* Unclassified
		15a. DECLASSIFICATION/DOWNGRADING SCHEDULE

16. DISTRIBUTION STATEMENT *(of this Report)*

Approved for public release; distribution unlimited.

17. DISTRIBUTION STATEMENT *(of the abstract entered in Block 20, if different from Report)*

18. SUPPLEMENTARY NOTES

HDL Project: A10819
DRCMS Code: 61110191A0011

19. KEY WORDS *(Continue on reverse side if necessary and identify by block number)*

Flaw detection
Crack detection
Opto-acoustics

20. ABSTRACT *(Continue on reverse side if necessary and identify by block number)*

An investigation of a laser flaw-detection system has been conducted. The technique replaces the piezoelectric transducers used in conventional flaw-detection systems with an optical system incorporating a pair of lasers. One laser generates a high-power pulse that strikes the test sample and generates a short-pulse acoustic wave in the sample. The second laser is used in an interferometer that monitors the surface motion. The advantages of this system over conventional techniques are its speed and flexibility. Since the system is remote—i.e., no physical contact is necessary—the sample could be optically scanned very rapidly. Also, there is no limitation on the size or shape of the test object as there might be with conventional methods.

DD FORM 1473 EDITION OF 1 NOV 65 IS OBSOLETE

The laser flaw-detection system has been evaluated for different types of flaw configurations. It was shown that internal flaws in a plane parallel to the surface with dimensions in the 2-mm range could easily be detected in metals. These flaws were simulated by drilling holes into the side of the sample. Improvements in the detection system and a decrease of the generating laser pulse width would allow detection of smaller flaws of this type. Also, flaws were detected that penetrate the sample normal to the surface in the same 2-mm size range. This type of flaw was simulated by cutting a slot into the surface of the sample. These flaws are inherently more difficult to detect because of the geometry. The technique has been shown to be feasible in a laboratory environment, but more evaluation is needed to determine the practicability under production-line conditions.

CONTENTS

FIGURES

CONTENTS (Cont'd)

1. INTRODUCTION

The best state-of-the-art methods for the detection of internal discontinuities, like cracks in solid materials, use ultrasonic waves. Typically, quartz or barium titanate piezoelectric transducers are used to generate the acoustic waves and to detect the reflections from the various discontinuities in the system. A critical aspect of this type of system is the coupling of the transducer to the material under test. Usually, the material is immersed in a liquid that increases the coupling efficiency. Reflections or echoes are then received from the metal-liquid interfaces at the sample surface and from the air-metal interfaces of any internal cracks or flaws. By observing the round-trip times of these echoes, one can distinguish the various interface reflections. This technique is currently in use in industry, but it has some serious drawbacks. The sample must be placed in a continuous-flow fixture that greatly increases the complexity of the scanning techniques required. This process is very time-consuming and is therefore not conducive to production-line testing.

A method for overcoming the difficulties of the conventional technique for flaw detection has been proposed by H. P. Kalmus of Harry Diamond Laboratories (HDL), and a preliminary evaluation of the proposed method has been made by Giglio.[1] Basically, the technique proposed involves replacing the generating and receiving piezoelectric transducers in presently used systems with a pair of lasers. One laser, generally a high-power pulse laser, is used to generate an acoustic wave in the sample under test, and the second laser records the motion of the surface of the sample caused by the acoustic waves generated by the first laser. A schematic of the proposed system is illustrated in figure 1. The fact that no physical contact with the sample under test is necessary is a major advantage over the presently used technique. An optical scanning system could be built that would provide rapid testing of similar items, and entire sample lots could be tested as they actually come off the assembly line.

[1] D. A. Giglio, *Preliminary Evaluation of a Proposed Laser-Operated Flaw Detection Technique,* Harry Diamond Laboratories, HDL-TM 73-32 (December 1973).

This report presents the results of a more extensive evaluation of the Kalmus flaw-detection proposal. A description is given of the acoustic-wave generating system and the investigation of the parameters that affect the pulse shape and amplitude of acoustic waves. Also, some theory on the generation of acoustic waves by the laser is presented. The investigation of a readout or recording system that uses a Michelson interferometer is also described. Some preliminary flaw-detection data on a polished metallic sample are discussed, and finally, data on the detection of flaws in artillery shells are presented.

2. ELECTRO-OPTICAL RECEIVER SYSTEM

An acoustic wave generated in a sample under test by a high-power laser pulse propagates as a longitudinal pressure wave. When this pressure wave strikes a boundary, the surface of the sample is displaced as the wave is reflected by the boundary. The surface motion at the boundary can be detected with a piezoelectric transducer that generates an electric signal proportional to the mechanical impulse. The motion of the surface can also be detected optically by using a laser beam in conjunction with an interferometer and some type of signal processing. Most of the work described in this paper involves the optical detection system, although some interesting data were also obtained using $BaTiO_3$ transducers.

The optical detection system chosen for this work was a Michelson interferometer. A schematic of the system is shown in figure 2. The laser beam enters the interferometer, where part of it is reflected towards a fixed mirror, M_2, by a half-silvered mirror, M_1. The remaining part of the beam proceeds to the sample under test (the sample acts as a movable mirror). The reflections from the sample and mirror are then recombined as shown in the figure. If the path difference between the two beams is not zero, then there is a phase difference between the two beams at the plane of the detector. In general, this leads to an interference pattern at the detector plane if the two reflecting surfaces are not perpendicular. Any motion of the sample under test will modulate this
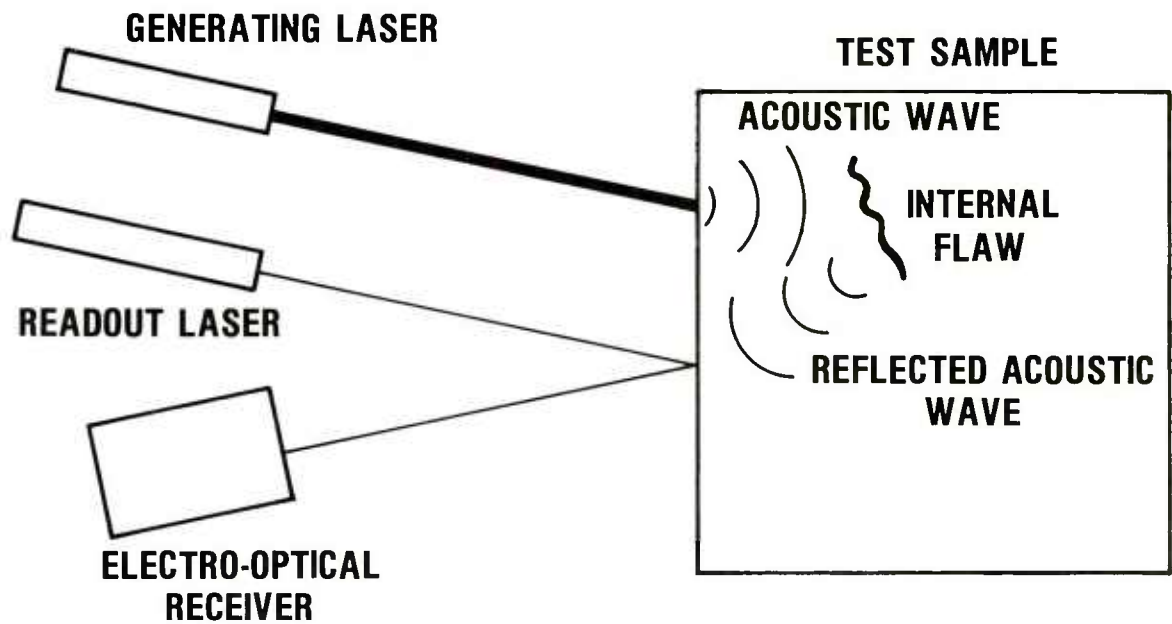
5

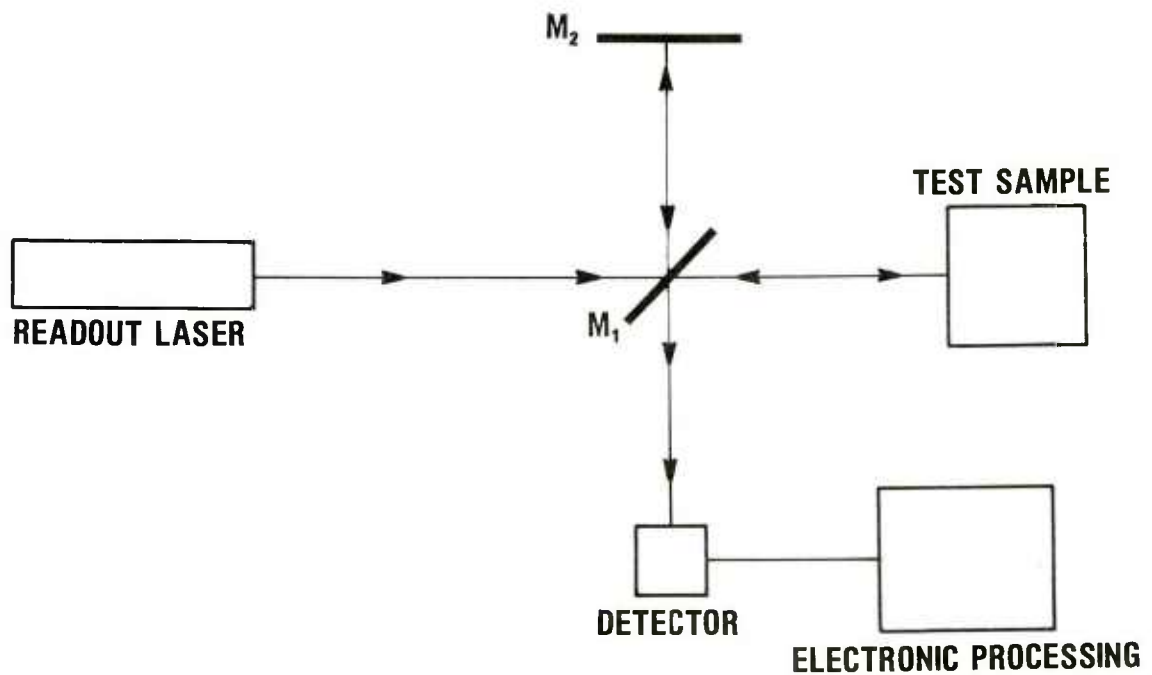Figure 1. Proposed laser flaw-detection system.

Figure 2. Simplified Michelson interferometer receiver system.

phase and therefore change the portion of the interference pattern viewed by the detector. The sample motion will therefore cause a change in the light intensity seen by the detector and a corresponding change in the electrical output.

The feasibility of this type of detection system for measuring small displacements or vibrations has been demonstrated by many authors.[1-4] To evaluate the intensity pattern produced at the detector plane, the alignment configuration shown in figure 3 is used. For simplicity, it is assumed that the misalignment angle θ between the test and reference beams is in one plane only. Using complex notation, we have for the test beam

$$\vec{E}_1 = K_1 E_0 e^{i(\omega t - k\{y_0 + 2[x_0 + \Delta x(t)]\})} \hat{i}_z \qquad (1)$$

and for the reference beam

$$\vec{E}_2 = \qquad\qquad\qquad (2)$$
$$K_2 E_0 e^{i\{\omega t - k[y_1 + x \sin\theta + (y_1 + y_0)\cos\theta]\}} \hat{i}_z \quad,$$

where E_0 is the electric field amplitude of the laser beam, K_1 and K_2 are proportionality constants which account for mirror losses, k is the wavenumber $2\pi/\lambda$, and $\Delta x(t)$ is the time-varying displacement of the sample under test. The detector current is proportional to the intensity, I, which is given by

$$I \propto E^* E$$

or

$$I \propto (K_1^2 + K_2^2) E_0^2 +$$
$$2K_1 K_2 E_0^2 \cos [kx \sin\theta + k(y_0 + y_1)$$
$$(\cos\theta - 1) + k(2y_1 - 2x_0 - 2\Delta x(t))] \; ;(3a)$$

[1] D. A. Giglia, Preliminary Evaluation of a Proposed Laser-Operated Flaw Detection Technique, Harry Diamond Laboratories, HDL-TM 73-32 (December 1973).

[2] H. A. Deferrari and F. A. Andrews, Laser Interferometric Technique for Measuring Small-Order Vibration Displacements, J. Acoustic. Soc. Am., 39 (1966), 979-980.

[3] S. Sizgaric and A. A. Gundjian, An Optical Homodyne Technique for Measurement of Amplitude and Phase of Subangstrom Ultrasonic Vibrations, Proceedings of IEEE (July 1969), 1313.

[4] C. R. Brown, G. R. Brown, and D. H. Niblett, Measurement of Small Strain Amplitudes in Internal Friction Experiments by Means of a Laser Interferometer, J. Physics, E: Scientific Instruments, 5 (1972), 966.

then

$$I \propto (K_1^2 + K_2^2) E_0^2 +$$
$$2K_1 K_2 E_0^2 \cos [C(x) - 2k\Delta x(t)] \quad, \qquad (3b)$$

where

$$C(x) = k[x \sin\theta + (y_0 + y_1)(\cos\theta - 1) +$$
$$(2y_1 - 2x_0)] \qquad . \quad (4)$$

Now let $\Delta x(t) = d\sin\Omega t$, where d is the amplitude of the displacement of the surface and Ω is the frequency of vibration. The signal current is proportional to the time-varying component, so

$$i_s \propto \cos [a \sin\Omega t - C(x)] \quad, \qquad (5)$$

where a is the modulation depth $\dfrac{4\pi d}{\lambda}$. By using trigonometric identities, we obtain

$$i_s \propto \cos (a \sin\Omega t) \cos C(x) +$$
$$\sin (a \sin\Omega t) \sin C(x) \qquad . \qquad (6)$$

Then, using the Bessel function expansions,[5]

$$\cos(a \sin\Omega t) =$$
$$J_0(a) + 2 \sum_{n=1}^{\infty} J_{2n}(a)\cos 2n\Omega t \qquad (7a)$$

$$\sin(a \sin\Omega t) =$$
$$2 \sum_{n=0}^{\infty} J_{2n+1}(a) \sin(2n+1)\Omega t \quad, \qquad (7b)$$

we get

$$\cos(a \sin\Omega t) = J_0(a) + 2J_2(a) \cos 2\Omega t +$$
$$2J_4(a)\cos 4\Omega t + \ldots \qquad (8a)$$

and

$$\sin(a \sin\Omega t) =$$

[5] G. N. Watson, A Treatise on the Theory of Bessel Functions, Cambridge Press (1952).

$$2J_1(a)\sin\Omega t + 2J_3(a)\sin 3\Omega t +$$

$$2J_5(a)\sin 5\Omega t + \ldots \qquad (8b)$$

Expanding each term, using

$$J_n(z) = \sum_{m=0}^{\infty} \frac{(-1)^m (1/2\ Z)^{n+2m}}{m!\ (n+m)!} \quad , \quad (9)$$

we get

$$J_0(a) = 1 - \frac{a^2}{4} + \frac{a^4}{64} + \ldots$$

$$J_1(a) = \frac{a}{2} - \frac{a^3}{16} + \frac{a^5}{384} + \ldots$$

$$J_2(a) = \frac{a^2}{8} - \frac{a^4}{96} + \frac{a^6}{3072} + \ldots$$

$$J_3(a) = \frac{a^3}{48} - \frac{a^5}{768} + \frac{a^7}{30720} + \ldots$$

$$J_4(a) = \frac{a^4}{384} - \frac{a^6}{7680} + \frac{a^8}{368640} \ldots \ldots (10)$$

If $a < 1$, all but the first term in each expansion can be neglected, although with considerable error for a close to one, then

$$i_s \propto \cos C(x) \left[1 + \left(\frac{a}{2}\right)^2 \cos 2\Omega t + \right.$$

$$\left. \frac{1}{12}\left(\frac{a}{2}\right)^4 \cos 4\Omega t + \ldots \right] + \qquad (11)$$

$$\sin C(x) \left[a\ \sin\Omega t + \frac{1}{3}\left(\frac{a}{2}\right)^3 \sin 3\Omega t + \ldots \right] .$$

Figure 3. Setup of interferometer for analysis.

8

If a narrowband detector centered at Ω is used, the signal current is given by $i_s \propto a \sin C(x) \sin\Omega t$. Also, if $a \ll 1$, a wideband detector can be used and the harmonics are negligible. For instance, if $a = 0.1$, the $\sin 3\Omega t$ term is proportional to 0.00002 and the $\cos 2\Omega t$ term is proportional to 0.0025. Also, for quadrature detection $C(x)$ is set as close to 90 deg as possible, so that the $\cos C(x)$ term becomes zero at the detector. Even at other positions, with the modulation depth small, the cosine term has no time-varying component.

The actual signal current will now be given by

$$I_s \propto S \ 2K_1K_2E_0^2 \int i_s dA \qquad (12a)$$

or

$$I_s \propto 2K_1K_2SE_0^2L \ \frac{4\pi d}{\lambda} \ \sin\Omega t$$

$$\int_{x_1}^{x_2} \sin C(x)dx \qquad , \qquad (12b)$$

where a detector that is rectangular with height L and length $x_2 - x_1$ is assumed, and S is the sensitivity of the detector. Evaluating the integral:

$$\int_{x_1}^{x_2} \sin C(x)dx = \int_{x_1}^{x_2} \sin k[x\sin\Theta +$$

$$(y_0 + y_1)(\cos\Theta - 1) + (2y_1 - 2x_0)]dx =$$

$$\int_{x_1}^{x_2} \sin k(x\sin\Theta + \psi)dx \qquad ,$$

where

$$\psi = (y_0 + y_1)(\cos\Theta - 1) + (2y_1 - 2x_0) .$$

Then

$$\int_{x_1}^{x_2} \sin C(x)dx =$$

$$\frac{2}{k\sin\Theta} \sin\left\{ \frac{k}{2} [(x_1 + x_2)\sin\Theta + 2\psi]\right\}$$

$$\sin\left\{ \frac{k}{2} [(x_2 - x_1)\sin\Theta]\right\} \qquad . \quad (13)$$

From these expressions, some conclusions can be drawn about the detector size and position for maximum signal. However, first consider the static fringe pattern, which can be plotted from equation (3b) with $\Delta x(t) = 0$. The fringe pattern exhibits a maximum when $C(x) = n\pi$, n even, so that the distance from one peak to another is given by finding the change in x, δx, required to cause a change in $C(x)$ of 2π, or

$$\Delta\left\{ k[x\sin\Theta + (y_0 + y_1)(\cos\Theta - 1) + (2y_1 - 2x_0)]\right\} = \Delta[k(x\sin\Theta + \psi)] = 2\pi.$$

Since x is the only variable, the separation in the maxima are determined by

$$k\delta x \ \sin\Theta = 2\pi \ \text{or} \ \delta x = \frac{2\pi}{k\sin\Theta} = \frac{\lambda}{\sin\Theta} \ .$$

This means a dark or light band is $\lambda/2\sin\Theta$ wide, which is one-half the distance between peaks. Furthermore, for the case $\psi = 0$, it is apparent that there is a maximum at $x = 0$, a minimum at $x = \lambda/2\sin\theta$, a maximum at $\lambda/\sin\theta$, and so on.

If we now examine equation 13, we see that the maximum signal is observed when

$$\frac{k(x_2 - x_1)}{2} \sin\Theta = \frac{m\pi}{2} \qquad m \ \text{odd}$$

and

$$\sin\Theta \ \frac{k(x_1 + x_2)}{2} + k\psi = \frac{m\pi}{2} \qquad m \ \text{odd};$$

or, with $m = 1$,

$$x_2 - x_1 = \frac{\lambda}{2\sin\Theta} \qquad ,$$

and, with $\psi = 0$,

$$\frac{(x_1 + x_2)}{2} = \frac{\lambda}{4\sin\Theta} \qquad .$$

Now $x_2 - x_1 = \ell$, the detector length, and $\frac{x_1 + x_2}{2}$ is the position of the center of detector.

Maximum signal is therefore observed when the detector is one static fringe width wide (one dark or one bright band), located halfway between a minima and maxima.

At the optimum position we get

$$I_s \propto 2K_1K_2SE_0^2L \frac{4\pi d}{\lambda} \sin\Omega t$$

$$\left[\frac{2}{k\sin\Theta} \sin\left(\frac{k\ell\sin\Theta}{2}\right) \right] \qquad (14)$$

or

$$I_s \propto 8\ K_1K_2SE_0^2A$$

$$\frac{\pi d}{\lambda}\ \sin\Omega t\ \frac{\sin\left(\dfrac{k\ell\sin\Theta}{2}\right)}{\dfrac{k\ell\sin\Theta}{2}} \qquad . \qquad (15)$$

For maximum signal, $\ell = \dfrac{\lambda}{2\ \sin\Theta}$, giving a signal current of

$$I_s \propto 16\ K_1K_2\ SE_0^2\ A\ \frac{d}{\lambda}\ \sin\Omega t. \qquad (16)$$

Therefore, if the modulation depth is small, the observed signal directly reproduces the vibrational motion of the sample. In experiments where a polished sample was used, the fringe pattern was positioned directly on the detector and the signal was observed in this manner. Figure 4 shows the variation of the intensity at the detector for various path differences between the test and reference beam.

In some experiments, diffuse or unpolished surfaces were used as the test object, and a focusing lens was required to collect the diffusely scattered radiation from the test sample. The
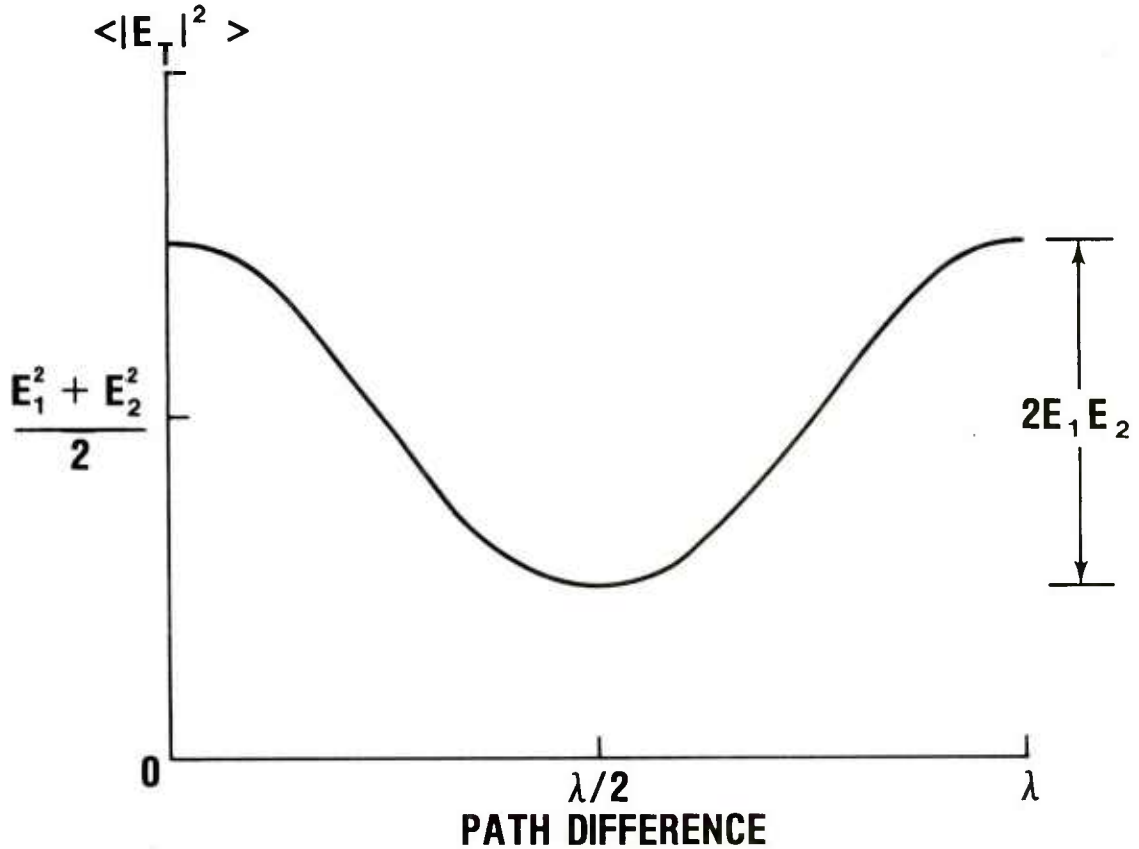
Figure 4. Intensity distribution at detector plane for setup of figure 3 with $\theta = 0$.

10

roughness of the test sample reduces the temporal and spatial coherence of the reflected radiation. This effectively reduces the signal-to-noise ratio at the detector, since the incoherent part of the reflected signal acts as background noise. Also in this case, the spherical aberration introduced by the lens created a circular fringe pattern at the detector. Since this was somewhat awkward to use, the misalignment angle was adjusted to give a parallel fringe pattern. We then placed a variable slit and lens in front of the detector and focused the fringe pattern after passing through the slit onto the detector. Using this technique we were able to get high sensitivities, even with the diffuse surfaces.

3. LASER SYSTEM FOR GENERATING ACOUSTIC WAVES

3.1 Laser Description

A commercial ruby laser was used to generate the acoustic waves. The laser has a 12.7 cm long by 0.95 cm diameter Brewster/Brewster rod. The laser was run in the Q-switched mode with a Pockel's cell Q-switch. The pulse energy varied between 0.9 and 1.4 J, and the pulse width was 50 ns at the half-power points. The power level varied from 18 to 28 MW. The unfocused spot size was 0.36 cm^2, which gives a power density from 50 to 78 MW/cm^2. Focused power densities up to 1 GW/cm^2 are easily obtained, but most of our experiments involved power densities under 500 MW/cm^2.

3.2 Radiation Pressure

The radiation pressure due to the reflection of the optical radiation from the sample for normal incidence can easily be calculated. The incident intensity at the sample is

$$I = Nh\nu, \qquad (17)$$

where N is the number of photons per second per unit area incident on the sample, h is Planck's constant, and ν is the frequency of the radiation. For a reflection coefficient, R, the momentum

transferred to the sample per photon upon reflection for a plane wave is

$$\Delta M = (1 + R)M = (1 + R) h/\lambda, \quad (18)$$

where λ is the wavelength. The total radiation pressure, which is the total change in momentum per unit area per unit time, is

$$P = (1 + R)Nh/\lambda \qquad , \qquad (19)$$

which with substitution from (17) gives

$$P = (1 + R)h/\lambda\left(\frac{I}{h\nu}\right) = (1 + R)I/c, \quad (20)$$

where c is the velocity of light.

The quantity I/c is simply the energy per unit volume of the laser beam, or the power density divided by c. For a power density of 500 MW/cm^2, typical for our experiments, and a reflection coefficient of 0.3, appropriate for stainless steel at 0.7 μm,[6] the radiation pressure is 2.0×10^5 dyn/cm^2.

3.3 Thermal Effects

The problem of thermoelastic stress production in solids has been discussed by many authors.[7-11] The problem consists of solving two differential equations. First, one solves the heat-flow equation to determine the temperature profile in the material generated by the incoming laser radiation. Then one must solve the equation relating the thermoelastic stress to the temperature profile.

[6] M. Born and F. Wolf, Principles of Optics, New York, Pergamon Press (1959), 619.

[7] J. F. Ready, Effects Due to Absorption of Laser Radiation, J. Appl. Phys., 36, 2 (February 1965), 462-468.

[8] J. C. Bushnell and D. J. McClaskey, Thermoelastic Stress Production in Solids, J. Appl. Phys., 39 (1968), 5541-5546.

[9] R. M. White, Generation of Elastic Waves by Transient Surface Heating, J. Appl. Phys., 34, (1963), 3559-3567.

[10] L. S. Gournay, Conversion of Electromagnetic to Acoustic Energy by Surface Heating, J. Acoustic. Soc. Am., 40, 6 (1966), 1322-1330.

[11] T. A. Zaker, Stress Waves Generated by Heat Addition in an Elastic Solid, J. Appl. Mech. (March 1965), 143-150.

Ready[7] has calculated the temperature distribution in a semi-infinite plane slab, assuming one-dimensional heat flow, no reradiation of energy, temperature-independent thermal properties, and that the liquid phase can be neglected. The heat production then takes the form

$$A(x,t) = I(t) \, \alpha e^{-x/\delta} \, , \qquad (21)$$

where δ is the optical penetration depth, α is the absorption coefficient, and $I(t)$ is the intensity distribution of the laser pulse in time. If one assumes that

$$I(t) = I_0 \text{ for } t \geq 0 \text{ and } I(t) = 0 \text{ for } t < 0,$$

one obtains the solution originally derived by Carslaw and Jaeger.[12]

$$T(x,t) = (2I_0\alpha\delta/K)(\kappa t)^{1/2}\text{ierfc}\left[x/2(\kappa t)^{1/2}\right]$$
$$- (I_0\alpha\delta^2 e^{-x/\delta}/K)$$
$$+ (I_0\alpha\delta^2/2K)e^{\kappa t/\delta^2 - x/\delta}\text{erfc}\left\{(\kappa t)^{1/2}/\delta - \left[x/2(\kappa t)^{1/2}\right]\right\} \qquad (22)$$
$$+ (I_0\alpha\delta^2/2K)e^{\kappa t/\delta^2 + x/\delta}\text{erfc}\left\{(\kappa t)^{1/2}/\delta + \left[x/2(\kappa t)^{1/2}\right]\right\} \, ,$$

where K is the thermal conductivity and κ the thermal diffusivity $K/\rho C$, with ρ the density, and C the specific heat of the material.

Ready then applies Duhamel's theorem[12] to get the temperature profile for a laser pulse with arbitrary shape. For appropriate $I(t)$'s representing real laser pulses, the temperature must be calculated by a numerical integration. However, to solve the thermoelastic stress equation, we need a closed-form solution for $T(x,t)$.

An alternative solution has been given by Bushnell and McCloskey.[8] They showed that the equations governing the propagation of stress waves generated in an isotropic medium due to illumination of a free surface by a laser pulse of energy density Q were

$$\Sigma(\xi,\tau) =$$
$$1/2 \int_{\xi-\tau}^{\xi} \frac{\partial}{\partial\tau}\left[\theta(y,\tau - \xi + y)\right]dy +$$
$$1/2 \int_{\xi}^{\tau+\xi} \frac{\partial}{\partial\tau}\left[\theta(y,\tau + \xi - y)\right]dy,$$
$$\tau < \xi \qquad (23a)$$

$$\Sigma(\xi,\tau) =$$
$$1/2 \int_{0}^{\xi} \frac{\partial}{\partial\tau}\left[\theta(y,\tau - \xi + y)\right]dy +$$
$$1/2 \int_{\xi}^{\tau+\xi} \frac{\partial}{\partial\tau}\left[\theta(y,\tau + \xi - y)\right]dy -$$
$$1/2 \int_{0}^{\tau-\xi} \frac{\partial}{\partial\tau}\left[\theta(y,\tau - \xi - y)\right]dy \, ,$$
$$\tau > \xi, \qquad (23b)$$

where $\Sigma = \delta\sigma/\gamma Q$ = normalized stress,

$\xi = x/\delta$ = normalized distance,

$\tau = c_0 t/\delta$ = normalized time,

$\theta = \rho C \delta(T - T_0)/Q$

= normalized temperature,

and σ, δ, ρ, c_0, C, and γ are the stress, penetration depth, density, longitudinal sound speed, specific heat, and Grüneisen constant of the absorbing medium, respectively, and y is a dummy integration variable.

A reasonable description of $\theta(\xi,\tau)$ can be obtained by assuming that the absorbed energy decays exponentially below the surface, and the pulse width is short enough so that heat conduction and conversion of thermal energy to acoustic energy can be neglected. Then

$$\theta(\xi,\tau) = e^{-\xi} \int_{0}^{\tau/\tau_0} g(y) \, dy \, , \qquad (24)$$

[7] J. F. Ready, *Effects Due to Absorption of Laser Radiation*, J. Appl. Phys., 36, 2 (February 1965), 462-468.

[8] J. C. Bushnell and D. J. McCloskey, *Thermoelastic Stress Production in Solids*, J. Appl. Phys., 39 (1968), 5541-5546.

[12] H. S. Carslaw and J. C. Jaeger, *Conduction of Heat in Solids*, Clarendon Press, Oxford, England (1959), 80; 30-31.

where $g(y)$ describes the laser pulse shape in normalized time and $\tau_0 = c_0 t_0/\delta$, the ratio of the acoustic penetration depth during the risetime t_0 of the laser pulse to the optical penetration depth. Using the practical envelope description,

$$g(y) = 2(e^{-y} - e^{-2y}) \quad ,$$

we get

$$\theta(\xi,\tau) = e^{-\xi}\left[1 - 2\exp\left(-\tau/\tau_0\right) + \exp\left(-2\tau/\tau_0\right)\right] \quad . \quad (25)$$

If we then substitute using this $\theta(\xi,\tau)$ in the equations for $\Sigma(\xi,\tau)$ which were calculated by Bushnell and McCloskey in a manner similar to that done by Giglio,[1] we get

$$\Sigma(\xi,\tau) = \frac{-4}{\tau_0^2 - 4}\,e^{-(\xi + 2\tau/\tau_0)} +$$

$$\frac{2}{\tau_0^2 - 1}\,e^{-(\xi + \tau/\tau_0)} + \quad (26a)$$

$$\frac{1}{(\tau_0 - 2)(\tau_0 - 1)}\,e^{-(\tau + \xi)} +$$

$$\frac{1}{(\tau_0 + 1)(\tau_0 + 2)}\,e^{\tau - \xi} \quad , \quad \tau < \xi \quad ,$$

and

$$\Sigma(\xi,\tau) = \frac{4}{\tau_0^2 - 4}\left[e^{-2(\tau - \xi)/\tau_0} - e^{-(\xi + 2\tau/\tau_0)}\right] +$$

$$\frac{1}{(\tau_0 - 2)}\frac{1}{(\tau_0 - 1)}\left[e^{-(\tau + \xi)} - e^{-(\tau - \xi)}\right] +$$

$$\frac{2}{\tau_0^2 - 1}\left[e^{-(\xi + \tau)/\tau_0} - e^{(\xi - \tau)/\tau_0}\right] \quad ,$$

$$\tau > \xi \quad . \quad (26b)$$

For distances large compared with the penetration depth, and making the substitution $\eta = \tau - \xi$, we have

[1] D. A. Giglio, *Preliminary Evaluation of a Proposed Laser-Operated Flaw Detection Technique*, Harry Diamond Laboratories, HDL-TM-73-32 (December 1973).

$$\Sigma(\eta) = \frac{+4}{\tau_0^2 - 4}\,e^{-2\eta/\tau_0} - \frac{2}{\tau_0^2 - 1}\,e^{-\eta/\tau_0} -$$

$$\frac{e^{-\eta}}{(\tau_0 - 2)(\tau_0 - 1)} \quad , \quad \eta > 0 \quad , \quad (27a)$$

and

$$\Sigma(\eta) = \frac{e^{\eta}}{(\tau_0 + 1)(\tau_0 + 2)} \quad , \quad \eta < 0 \quad . \quad (27b)$$

We see that the stress wave has assumed a traveling form, since

$$\eta = \tau - \xi = \frac{(c_0 t - x)}{\delta} =$$

$$\frac{1}{2}\left(\omega_s t - k_s x\right) \quad , \quad (28)$$

where ω_s and k_s are a normalized frequency and wavenumber dependent on the penetration depth δ. To further reduce these equations we need to estimate δ.

For nonmagnetic steel, the penetration depth for a frequency of 10^{14} Hz is $\simeq 10^{-6}$ cm. This means, with a 50-ns risetime pulse, that

$$\tau_0 = \frac{c_0 t_0}{\delta} = 2.9 \times 10^4 \quad .$$

We can then write

$$\Sigma(\eta) = +\frac{4}{\tau_0^2}\,e^{-\eta/\tau_0} - \frac{2}{\tau_0^2}\,e^{-\eta/\tau_0} -$$

$$\frac{e^{-\eta}}{\tau_0^2} \quad , \quad \eta > 0 \quad , \quad (29a)$$

$$\Sigma(\eta) = \frac{e^{\eta}}{\tau_0^2} \quad , \quad \eta < 0 \quad . \quad (29b)$$

The above equations indicate that the largest value of $\Sigma(\eta)$ is given by

$$\Sigma_{max} = 1/\tau_0^2 \quad ,$$

or in terms of the stress,

13

$$\sigma_{\max} = \frac{\gamma Q}{\delta \tau_0^2} = \frac{\gamma Q \delta}{(c_0 t_0)^2} \qquad , \qquad (30)$$

where Q is the energy density of the illuminating pulse. More correctly, we must replace Q by Q $(1 - R)$, which corresponds to the absorbed energy. Thus, the peak stress is given by

$$\sigma_{\max} = Q \ (1 - R) \ \frac{\delta}{(c_0 t_0)^2} \qquad , \qquad (31)$$

where we have taken $\gamma = 1$ for steel. Also, $Q = P_0 t_0 / A$, where P_0 is the laser peak power and A the beam area. Therefore,

$$\sigma_{\max} = \frac{P_0 (1 - R) \ \delta}{A \ c_0^2 t_0} \qquad , \qquad (32)$$

and with

$$\frac{P_0}{A} = 500 \ \frac{MW}{cm^2}$$

$$R = 0.3$$

$$c_0 = 6 \times 10^3 \ m/s$$

$$t_0 = 50 \times 10^{-9} \ s$$

$$\delta = 10^{-6} \ cm \qquad ,$$

we get $\sigma_{\max} = 2 \times 10^5$ dyn/cm². This value is about twice the value obtained for the radiation pressure. For most reasonable values of R, the thermal pressure is somewhat larger than the radiation pressure.

3.4 Blow-Off Material Pressure

The vaporization of material from the target during the laser pulse can contribute strongly to the pressure wave generated in the sample under test. The material removed from the sample during the laser pulse imparts a momentum to the sample that is equal in magnitude and opposite in sign to that of the blow-off material. This, in turn, produces a pressure wave in the sample. The depth of material removed from a target due to vaporization by Q-switched laser pulses has been reported

in the literature.[13] A value of 1.1 μm for a stainless-steel target and a power density of 10^9 W/cm² is typical. In our experiments, a power density of 5×10^8 W/cm² produces the largest signal; the depth of material removed per shot is therefore $\simeq 0.5$ μm.

A simple estimate of the pressure exerted on the sample by the vaporized material can be made if the volume of material removed and the velocity of this material is known. Weichel and Avizonis[14] have measured the plasma plume velocity observed when illuminating a carbon target. Their measurements showed that the initial velocity of the plume was approximately the same for any energy density which produced vaporization. At higher energy densities, the plume velocity increases from the initial value due to the absorption of the laser radiation and subsequent heating of the plasma. The energy densities used in our experiments were only slightly above the point where vaporization occurs, so the initial vaporization velocity will be used in our calculations.

Weichel and Avizonis found that the initial velocity approached the normal vaporization velocity, which can be estimated from

$$V_i = \left(\frac{4}{3} \ CT_s\right)^{1/2} \qquad , \qquad (33)$$

where C is the specific heat and T_s is the sublimation temperature of the target. For steel, the sublimation temperature will be taken to be $\sim 3000°K$, so that, with C = 0.107 cal/g°K, we get $V_i = 2 \times 10^5$ cm/s. The volume of material removed at 500 MW/cm² can be calculated from the vaporized depth (0.5 μm) and the spot area (0.055 cm²). The momentum of the blow-off material is then given by

$$M_B = V \ V_i \rho \quad , \qquad (34)$$

where V is the volume and ρ the target density.

[13] J. F. Ready, Effects of High-Power Laser Radiation, New York, Academic Press (1971), 111, 161-206.

[14] H. Weichel and P. V. Avizonis, Expansion Rates of the Luminous Front of a Laser-Produced Plasma, Appl. Phys. Lett., 9, 9 (1966), 334-337.

With $V = 2.75 \times 10^{-6}$ cm^3 ,

$V_i = 2 \times 10^5$ cm/s , and

$\rho = 7.75$ g/cm^3 ,

M_B would be 4 dyn-s. To obtain the pressure, we divide by the pulse width and area. The blow-off pressure is then 1.5×10^9 dyn/cm^2. Measurements of the momentum transferred to a sample from surface vaporization have been reported in the literature. Gregg and Thomas[15] reported a momentum transfer of 5/dyn-s/J for an aluminum target using a 7.5-ns ruby laser pulse with peak power density in the range of 500 MW/cm^2. The pulse energy was 0.11 J, giving a total impulse to the target of 0.55 dyn-s. Neuman,[16] in a similar experiment, measured impulses of 0.17 dyn-s for both aluminum and cold rolled steel targets. The peak power density was 800 MW/cm^2, the pulse width was 50 ns, and the total energy was 0.3 J.

To convert these impulse values to pressure at the surface of the sample, we divide by the pulse length and spot size. For comparison to the values calculated previously for radiation and thermal pressure we also normalize to the same total energy. With a 1-J, 50-ns pulse and a spot size of 0.4 cm^2, the pressures for the cases measured by Gregg and Thomas and Neuman would be 2.5×10^9 dyn/cm^2 and 2.8×10^8 dyn/cm^2, respectively. The values are much higher than the estimated radiation pressures and in reasonable agreement with the value obtained from the estimate based on material removal alone.

A significant difference exists between our experiments and those done by Gregg and Thomas and Neuman. Their measurements were performed in a vacuum whereas ours were in air. The presence of air at the focal position of the laser pulse could increase the degree of plasma formation due to the higher density of atoms in the plasma volume. These atoms can contribute to the cascade process involving free electrons that takes place during plasma formation. Once a significant amount of material is vaporized, the plasma will shield the sample from the later parts of the laser pulse. The absorption of the laser pulse by the plasma will increase the plasma density and reduce the measured momentum transfer. Therefore, we might expect slightly lower numbers for our experiments. As indicated by Gregg and Thomas[15] and in Neuman,[16] the effect of plasma formation becomes important at power levels greater than 1 GW/cm^2, even in a vacuum. As the power density increases beyond this point the impulse delivered to the sample decreases. The power level of peak momentum transfer is probably lower in a non-evacuated system.

If the blow-off material pressure is compared to the thermal and radiation pressures as calculated at 500 MW/cm^2, the blow-off pressure is between three and four orders of magnitude higher than the thermal or radiation pressure. The blow-off material pressure is easily the dominant pressure at 500 MW/cm^2. However, if the power density is reduced by 10, the thermal and radiation pressures drop linearly while the blow-off pressure, which depends on the amount of ionized material ejected from the surface, drops much faster. The experimental observation of this effect will be discussed in a later section in some detail.

3.5 Estimation of Expected Surface Motion

To calculate the motion of the surface of the sample caused by the impulsive force delivered by the laser pulse, a few assumptions are necessary. First, we assume that the pressure is uniformly exerted on the sample over the half-power pulse width of the laser pulse. Secondly, we assume that the strained material depth is equal to the depth of penetration of the resulting acoustic wave during the laser pulse duration. We also assume that the acoustic wave generated in this manner is a plane wave. This implies that the stress and strain in the sample are related by

$$e_{xx} = \frac{1}{C_{11}} P \quad , \qquad (35)$$

[15] D. W. Gregg and S. J. Thomas, Momentum Transfer Produced by Focused Laser Giant Pulses, J. Appl. Phys., 37 (1966), 2787.

[16] F. Neuman, Momentum Transfer and Cratering Effects Produced by Giant Laser Pulses, Appl. Phys. Lett., 4 (1964), 167.

where e_{xx} = strain,

P = pressure, and

C_{11} = compliance coefficient.

Let us assume that $P = 10^8$ dyn/cm^2, due to blow-off for a power density of 500 MW/cm^2. This is a conservative estimate, since the value is somewhat lower than that estimated from the literature discussed in the previous section. This gives, with $C_{11} = 2.4 \times 10^{12}$ dyn/cm^2 for steel,[17] a value for e_{xx} of 4.2×10^{-5}.

To calculate the motion of the front surface of the sample, we multiply the strain by the penetration depth of the stress pulse, which is just

$$P_d = c_0 t \quad , \qquad (36)$$

where $c_0 = 5.92 \times 10^5$ cm/s, the longitudinal sound speed for steel,[6] and $t = 50 \times 10^{-9}$ s, so that

$$P_d = 3.0 \times 10^{-2} \text{ cm} \quad .$$

Therefore,

$$\Delta\ell = P_d \, e_{xx} = 1.2 \times 10^{-6} \text{ cm} \quad , \text{ or}$$

$$\Delta\ell = 0.012 \, \mu\text{m for } F = 10^8 \text{ dyn/cm}^2 \quad .$$

Assuming the minimum blow-off material pressure from the literature of $F = 2.8 \times 10^8$ dyn/cm^2, we would get a $\Delta\ell = 0.034$ μm. It must be stressed that this motion is for the front surface only. It also implies that all momentum transferred to the sample is contained in a narrow acoustic pulse. Divergence or beam spread of the acoustic wave and attenuation in the material results in a smaller $\Delta\ell$ at the point of observation. In our readout system, we used both a NeHe laser and an Argon laser. The operating wavelengths were 632.8 and 514.5 nm, respectively. With these lasers and a maximum surface motion of 0.034 μm, the maximum signal for the direct wave would be in the $\lambda/15$ range. The intensity of

the acoustic wave scattered from a flaw is less, of course, since only part of the acoustic wave is scattered. The observed signal from a flaw is a complicated function of the flaw size, position, and geometry. A detailed theoretical evaluation of these scattering effects is beyond the scope of this report.

3.6 Analysis of Plasma Effects

A high-density plasma is created when the laser beam vaporizes the surface of the test sample. The density and velocity of this plasma can significantly affect the amount of radiation reaching the surface and the total amount of material removed. Ready[13] presents a comprehensive review of the experimental and theoretical work which has been done in this area. Estimates of the plasma density and velocity for our experiments are based on his book.

The plasma electron density determines the frequency of radiation which can be transmitted through the plasma. The plasma frequency is given by $\nu_p = 8.9 \times 10^3 \, n_e^{1/2}$, where n_e is the electron density. If $\nu > \nu_p$ the incident radiation is reflected by the plasma, and if $\nu < \nu_p$ the radiation is transmitted. For the ruby wavelength, the radiation would be reflected if $n_e > 2.4 \times 10^{21}$ cm^{-3}. The electron density can approach 10^{19} cm^{-3} for short times with lasers similar to ours. The very high velocity of plasma expansion, typically 10^6 to 10^7 cm/s, would reduce the electron density quickly. It is obvious that the electron density does not approach that needed to reflect the ruby light in our case.

Experimental evidence[13] shows that the plasma is accelerated during the laser pulse. This means that although the vapor leaves the surface at a velocity commensurate with the normal vaporization velocity due to boiling, the velocity can increase by orders of magnitude after leaving the surface. This increase in velocity is due to the absorption of photons by free electrons in the inverse Bremsstrahlung process. The electrons are raised to a higher state in the continuum. Weichel

[6]M. Born and F. Wolf, Principles of Optics, New York, Pergamon Press (1959), 619.

[17]S. P. Clark, ed., Handbook of Physical Constants, Geological Soc. of America (1966).

[13] J. F. Ready, Effects of High-Power Laser Radiation, New York, Academic Press (1971), 161-206, 111.

and Avizonis[14] have shown that for an energy density of 70 J/cm^2, the plasma expansion velocity can increase by as much as five times. This absorption would reduce the amount of laser light reaching the sample. A rough estimate of the plasma absorption constant can be made by using the formula

$$K_\nu = 3.69 \times 10^8 \, (Z^3 n_i^2/T^{1/2}\nu^3)$$

$$(1 - e^{-h\nu/K_BT}) \quad , \qquad (37)$$

where Z is the average charge per ion, n_i the density of ions, T the temperature of the plasma, and K_B the Boltzmann constant. Measured plasma temperatures for a power density of 5×10^8 W/cm^2 are about 5 eV. We will assume that n_e is 10^{19} cm^{-3}. For iron, which has 26 electrons, the outside shell electrons are very loosely bound. Spectra of Fe(XII) and Fe(XIII) have been observed in a plasma generated by a laser pulse striking an iron target. Experiments also indicate that the highly ionized states appear early in the plasma, whereas the lower ionized states appear later. Therefore, we will assume that Z is 10. This would make $n_i = 10^{18}$ cm^{-3} for $n_e = 10^{19}$ cm^{-3}. K_ν then equals 6.3 cm^{-1}. This estimate was made from data that were taken in a vacuum.[13] Our measurements were made at normal pressure; the presence of air at the focal position could increase the plasma electron density because of the extra ions available to feed the cascade process. Therefore, if the plasma was 1 mm thick, about 50 percent of the remaining part of the laser pulse would be absorbed. This absorption of the laser light would increase the plasma temperature, which would in turn heat the sample until it dissipated. Thus, if you were monitoring the energy transfer to the sample, you would first see an energy deposition which followed the laser pulse until vaporization occurred. At this point, depending on the density of this resulting plasma, there would be a decrease in the absorbed energy while the plasma was heated. The plasma would then transfer heat to the sample by radiation and conduction before it completely dissipated.

[13] J. F. Ready, Effects of High-Power Laser Radiation, New York, Academic Press (1971), 111, 161-206.

[14] H. Weichel and P. V. Avizonis, Expansion Rates of the Luminous Front of a Laser-Produced Plasma, Appl. Phys. Lett., 9, 9 (1966), 334-337.

4. EXPERIMENTAL SETUP AND RESULTS

4.1 Transducer Experiments

Experiments were conducted to characterize the acoustic waves generated in a steel sample by a high-powered laser beam. A schematic of the experimental setup is shown in figure 5. The sample used most often was a steel cylinder 5 cm in diameter and 2.5 cm thick. A BaTiO$_3$ transducer was placed on the back face of the sample under test. The transducer had a diameter of 6.35 mm and a thickness of 3.17 mm, with a thickness-mode resonance of 800 kHz and a radial-mode resonance of 400 kHz. The transducer was placed against the back of the steel sample with silicone grease, and pressure was applied to its back face by a rubber-covered screw. The sample was grounded to the outer shield of a 50-Ω cable while the center conductor of the cable was conected to the back face of the transducer. The electrical load was supplied by a termination at the oscilloscope.

The loading conditions on the transducer have a large effect on the Q of the transducer and therefore its bandwidth. Huester and Bolt[18] have shown that by loading a transducer with steel and using a rubber backing, the mechanical Q of the transducer can be reduced drastically, and by terminating the transducer in a low impedance, the electrical Q can also be reduced. Figure 6 shows the effect of changing the load impedance from 1 MΩ to 50 Ω. In figure 6(a) the signal received by the transducer terminated in 1 MΩ is shown for a laser pulse of 0.9 J or 50 MW/cm^2. The laser pulse is incident on the front face of the sample near the beginning of the trace. Its position is indicated by the ringing due to pickup in the input cable caused by the high voltage discharge of the laser. The delay in the signal from the laser pulse to the acoustic pulse is due to the transit time of the acoustic wave through the sample. In figure 6(b) the same pulse is shown with the cable terminated with a 50-Ω load. Notice that the signal level is decreased and that the pulses have become much

[18] T. F. Huester and R. H. Bolt, Sonics, New York, John Wiley and Sons Inc. (1955), 106-109.
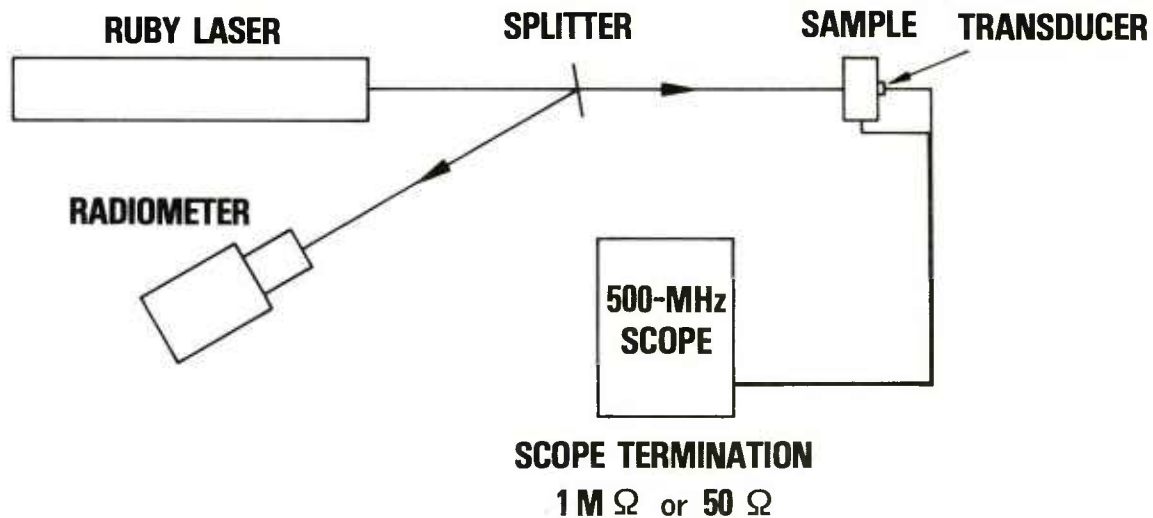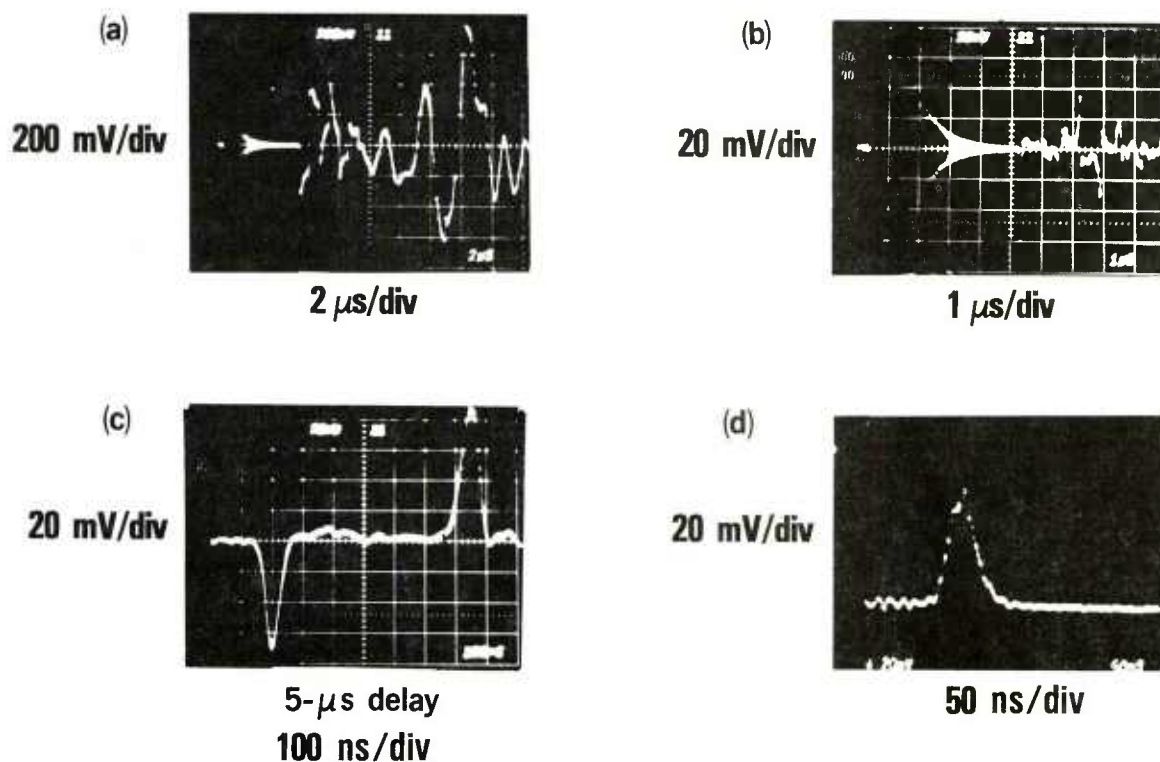
Figure 5. Experimental setup for transducer measurements.

Figure 6. Received signals using BaTiO$_3$ transducer for different loading conditions: (a) 1-MΩ termination, (b) and (c) 50-Ω termination, (d) incident laser pulse.

narrower. Figure 6(c) shows the first two pulses in figure 6(b) on an expanded time scale (100 ns/div). The first pulse is a good reproduction of the incident laser pulse, a trace of which is shown in figure 6(d). The second pulse is the reflection of the acoustic wave from the back face of the transducer. The reason for the increase in apparent signal level for the reflection is not clear, but we suspect it is caused by the different loading conditions at the back surface. Since the pulse shape is a good reproduction of the laser pulse, it is clear that the effective bandwidth of the transducer has been greatly increased by loading it with 50 Ω, and it is also evident that the ringing in the transducer seen in the later part of figure 6(a) has been almost completely eliminated. The transducer signal observed using a 50-Ω load indicates that, with a 50-MW/cm^2 pulse of 0.9 J incident on a piece of steel, the resulting acoustic wave shape closely approximates that of the incident laser pulse. This will be discussed in more detail later, along with some other acoustic wave characteristics.

4.2 Direct Transmission Interferometer Experiments

The electro-optical receiver system was discussed in some detail in a previous section. In this section the experimental results for the detection of transmitted acoustic waves using the interferometer will be discussed. In all cases the sample was a steel cylinder 2.5 cm thick and 5 cm in diameter, with the back face ground and polished. The polished side was used as one mirror of the interferometer. The experimental setup is shown in figure 7. A narrowband filter precedes the detector amplifier assembly which is a commercial silicon avalanche detector module. The detector amplifier's maximum sensitivity is 3.7×10^4 V/W at 900 nm and slightly less at 630 nm. The output from this assembly was split into two parts as shown in the figure. The high-frequency output was fed directly to a 500-MHz bandwidth oscilloscope, while the dc output was fed to another oscilloscope for monitoring the fringe position at the detector. A micrometer adjustment on the interferometer allowed positioning of the fringe pattern so that the detector was at the most sensitive position, that is, halfway between a minima and maxima. The interferometer was typically set up so that the difference from a minima to a maxima was between 1 and 1.5 V. A complete swing from a minima to a maxima corresponds to a phase difference of 180 deg or a movement at the sample of 1/4 of a wavelength, or 0.158 μm when using the HeNe laser. Experiments were conducted to characterize acoustic wave shape, amplitude, and beam spread as a function of generating laser parameters.

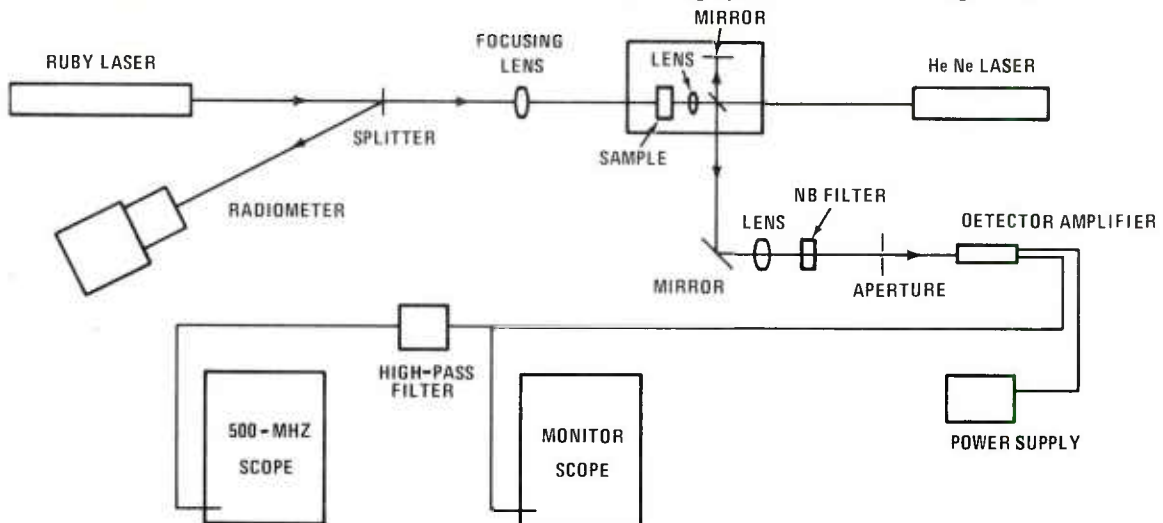A typical signal from the electro-optical receiving system is shown in figure 8. The initial

Figure 7. Experimental setup of direct transmission interferometer measurements.

part of the pulse corresponds to the acoustic wave generated by the expulsion of material from the surface, while the slow rising wave that follows is due to heating effects in the material. To measure the angular spread of the acoustic wave in the sample the interferometer was set up with the generating spot and readout spot centered on opposite sides of the sample. By translating the focusing lens shown in figure 7, the generating spot could be moved across the sample. By varying the distance between the focusing lens and the sample, the generating spot size could be varied. Figure 9 shows a plot of the initial peak value for two generating spot sizes as a function of position. The spot diameters in the scan direction are 5.6 and 2.4 mm. The widths of the acoustic beams to the half-peak points for the two traces are 8.1 and 13.8 mm, respectively. This is what one would expect, since the smaller the source, the closer it approximates a point source, and the more spherical the wave fronts become. This indicates that the smaller the generating spot, the larger the angular spread and the faster a sample could be scanned, but at the expense of requiring a greater detection system sensitivity.

Other parameters of interest are the acoustic wave shape and amplitude. With the generating spot centered with respect to the readout spot, the power density at the sample was varied in two ways. In one case, the ruby laser was filtered to vary the energy at the sample while the spot size was held constant. This was done for two spot sizes. The curves in figure 10 were obtained with the 0.3 cm^2 unfocused incident beam. The initial peak level is the maximum level of the initial peak shown in figure 8, while the slow peak is the maximum level of the slower wave shown in the same figure. The fast wave increases quite drastically at 45 MW/cm^2; this power density corresponds to the point where material is starting to be removed from the sample. A similar series of data points was obtained with an incident beam spot area of 0.06 cm^2. The maximum power density in this case was 510 MW/cm^2. Figure 11 shows some initial pulse signals for various power densities. Note that for power densities above 150 MW/cm^2, the signal has a different shape. The fast rise of the pulse is the same, but the signal does not return to the baseline level. Figure 12 shows a plot of the initial peak signal level and the signal level at the third graticule line or 600-ns point plotted against power density for these data.

In the second case a set of data was taken with constant energy but varying spot sizes. Figure 13 shows some typical signal returns for power densities from 500 to 1000 MW/cm^2. Notice that for some of the higher levels, the initial peak is not easily visible and the signal level actually rises to higher values later. Figure 14 is a plot of these data in the same format as figure 12. It is evident that the signal level for both the initial peak and 600-ns point drops steadily above 600 MW/cm^2. As discussed previously, this is due to the formation of a plasma at these high-power densities; the plasma becomes highly absorbing to the laser radiation
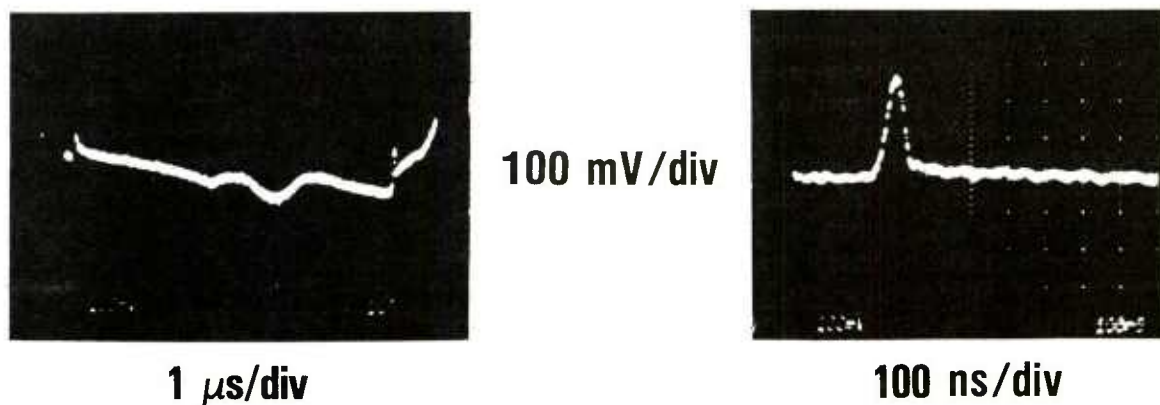
100 mV/div

1 μs/div   **100 ns/div**

Figure 8. Typical acoustic waves as detected with interferometer.
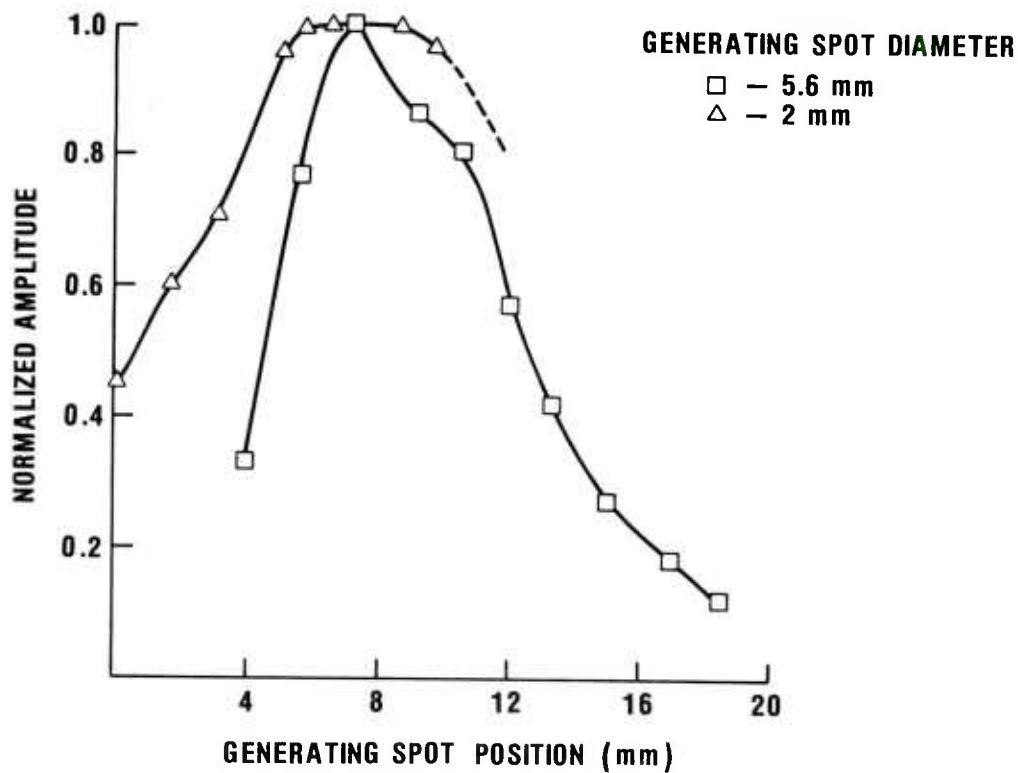
20

Figure 9. Acoustic wave beam width at back face of sample for two generating spot diameters. The measured beam widths were 8.1 and 13.8 mm for 5.6- and 2-mm diameter spots, respectively.
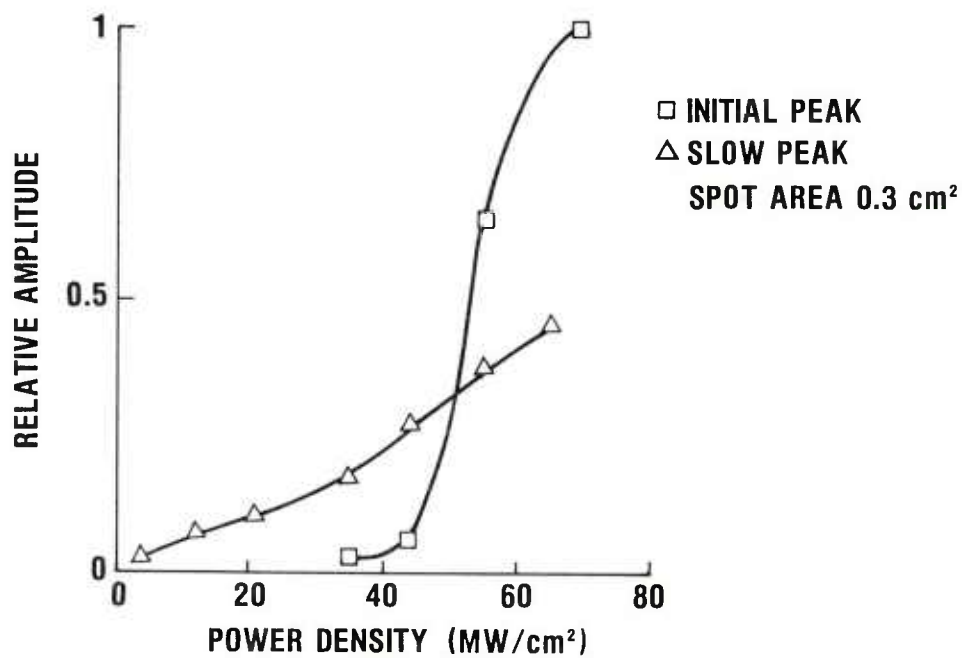

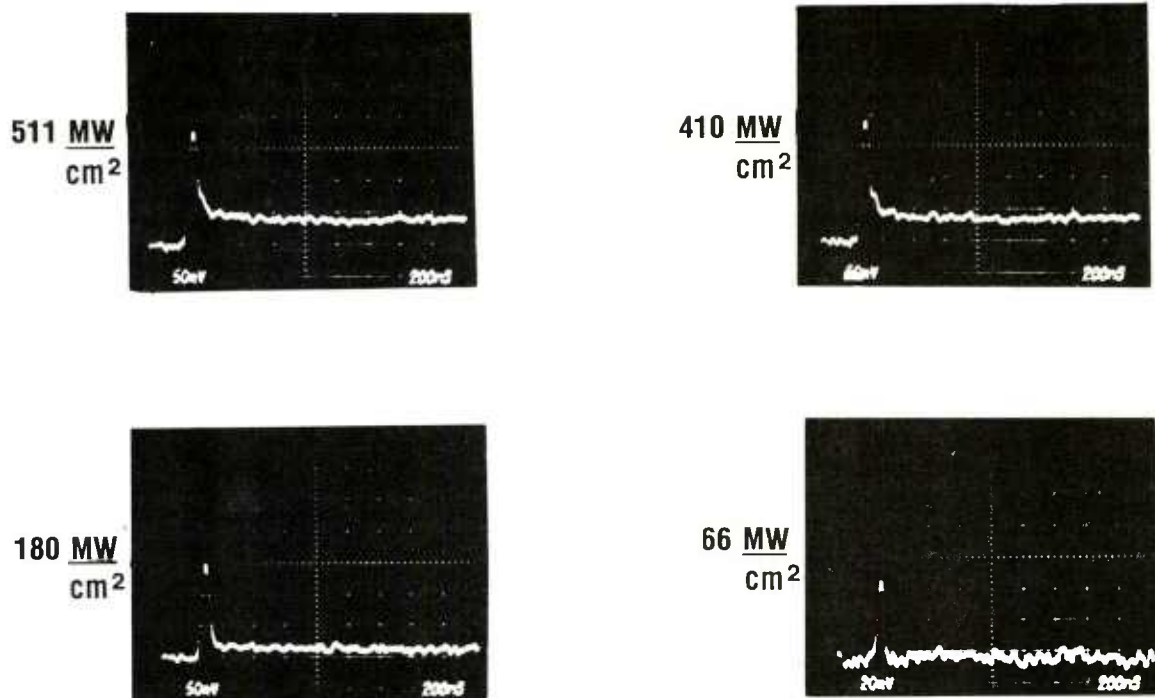Figure 10. Acoustic wave signal level versus power density for a constant generating spot size.

Figure 11. Oscilloscope photographs of received acoustic waves for various power densities, keeping generating spot size constant. The vertical scales are 50 mV/div for all but the 66 MW/cm² case, when it is 20 mV/div. Horizontal scales are all 200 ns/div.
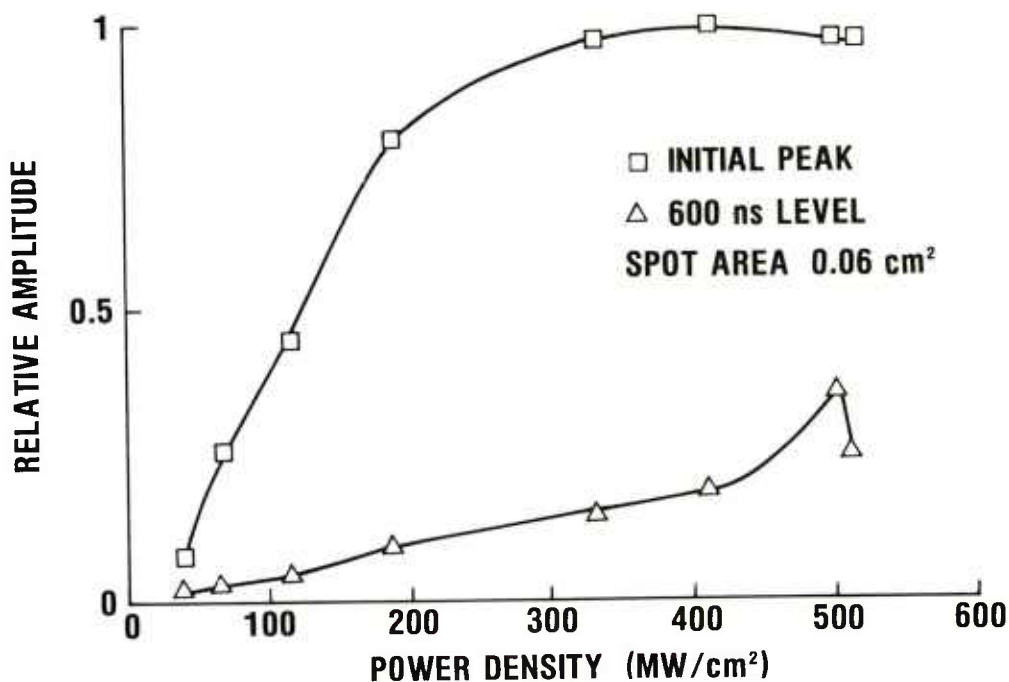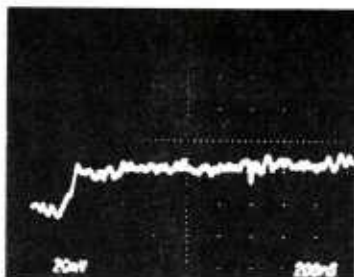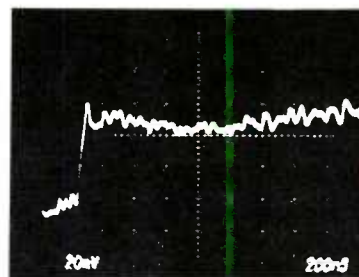

Figure 12. Observed acoustic wave amplitude versus power density for two different positions on oscilloscope traces. Data were obtained using reduced spot size from that for data of figure 10.
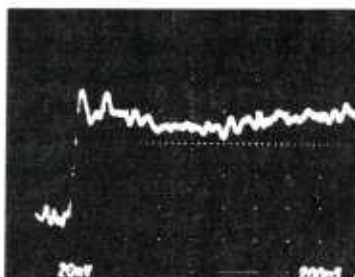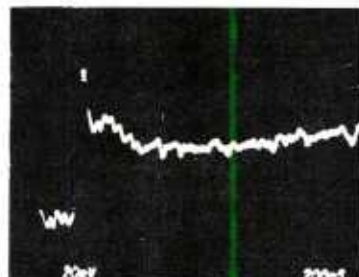
22

Figure 13. Oscilloscope photographs of acoustic waves obtained by keeping pulse energy constant and varying generating spot size. The scales are 20 mV/div and 200 ns/div.
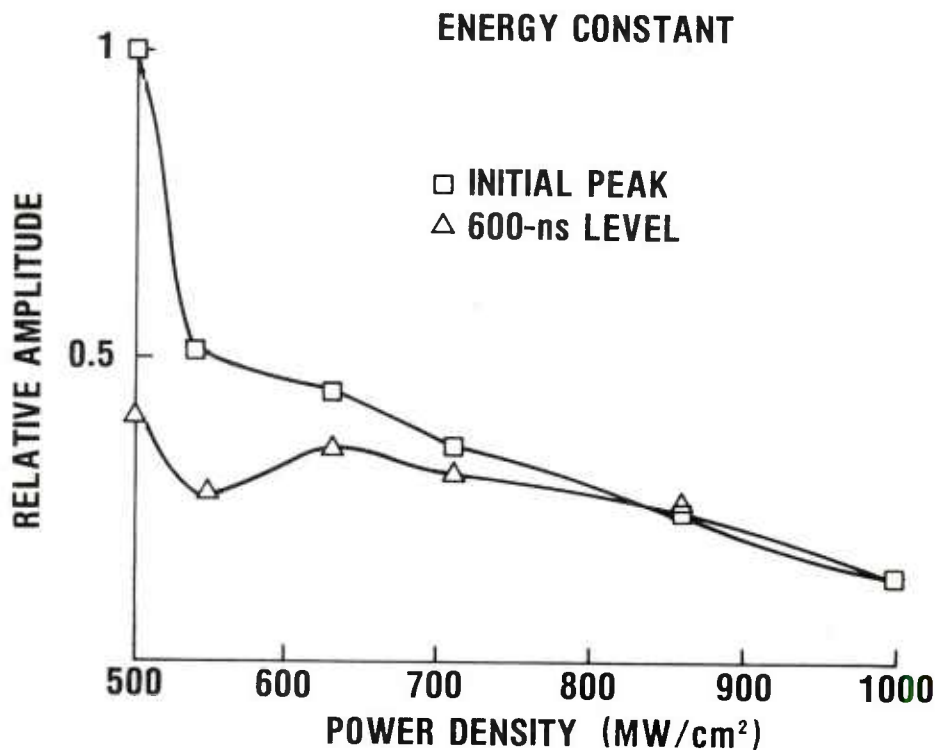

Figure 14. Signal amplitude versus power density for two positions as in figure 12.

23

and thereby shields the sample from the latter part of the laser pulse. The plasma is heated while absorbing the laser pulse, and it in turn transfers some of the heat to the sample until it dissipates, giving the high levels at the 600-ns point.

Figures 10, 12, and 14 cannot be compared directly because of the various spot sizes. For a more detailed evaluation of the effects of power density on acoustic wave amplitude, a much higher power laser would be needed so that an entire range of power densities of interest could be scanned without varying the spot size.

A comparison between calculated and measured surface motion is difficult to make. Data in the literature indicate that the maximum impulse is delivered to a target for power levels of about 500 MW/cm^2.[14] These data were taken by varying laser energy while keeping spot size constant at 0.03 cm^2. A typical surface motion for this power density and spot size in our experiments was 0.02 μm, compared to a calculated value at the front surface of 0.034 μm (sect. 3.9). By comparing the amplitude of the directly transmitted wave with that of the wave which traverses the sample three times, the one-way transmission was calculated to be 56 percent. This would account for the difference in the calculated front surface motion and the observed surface motion at the back face.

The maximum value of the initial peak signal observed in our experiments was for a power density of 70 MW/cm^2. This is a lower power density than reported in the literature but with the same incident energy and a larger spot size. It is the maximum power density that we could obtain with this spot size. Increasing the power density by reducing the spot size reduced the signal because of a combination of two factors. First, the smaller spot size creates a less collimated acoustic beam in the sample. Second, the higher power density increases the amount of plasma formation, which means that a smaller portion of the energy is used to create the acoustic wave. The surface displacement at the 70 MW/cm^2 power density was 0.03 μm at the

back face. Considering the assumptions and approximations made in calculating the surface displacement, along with the range of data in the literature, the values obtained are in good agreement with calculated values.

4.3 Reflection and Flaw-Detection Experiments

In order to demonstrate the feasibility of a remote flaw-detection system where the acoustic waves are both generated and detected by laser beams, the experimental setup shown in figure 15 was used. To increase the dynamic range and sensitivity of the readout system over the system shown in figure 7, an Argon laser operating with a single-frequency etalon was used instead of a HeNe laser. Its power is variable up to 1 W at the 514.5-nm line. The detector amplifier was changed so that the detector fed into two separate amplifiers, a low-frequency amplifier for displaying the fringe position and a wide-bandwidth amplifier (100 kHz to 50 MHz) for displaying the acoustic pulses. The sensitivities are 1.6×10^4 V/W for the wideband amplifier and 1.4×10^4 V/W for the low-frequency amplifier. The main advantage of this system is that the wideband amplifier can swing both positive and negative without saturating. The experiments involving the side-by-side generating and detecting system were conducted to characterize the signal generated on the face of the sample. The same 2.5-cm thick, 5-cm diameter, polished-steel sample discussed in section 4.2 was used. The signal shown in figure 16 was typical of those obtained. The separation between the generating and readout spots in this case was 8.6 mm. The ringing at the beginning of the trace is electrical pickup. The first pulse, which is somewhat square, is due to a surface wave propagating from the generating spot to the readout spot. The narrow pulse at the center of the picture corresponds to the reflection of the bulk wave from the back face of the sample. The next large peak is due to reflections of the surface waves from the sides of the sample. A flaw in the sample would be visible somewhere before the first narrow spike at the center of the picture. Its exact location on the trace would depend, of course, on the precise location of a flaw, but the reflection from the flaw would show

[14] H. Weichel and P. V. Avizonis, *Expansion Rates of the Luminous Front of a Laser-Produced Plasma, Appl. Phys. Lett., 9, 9, (1966), 334-337.*
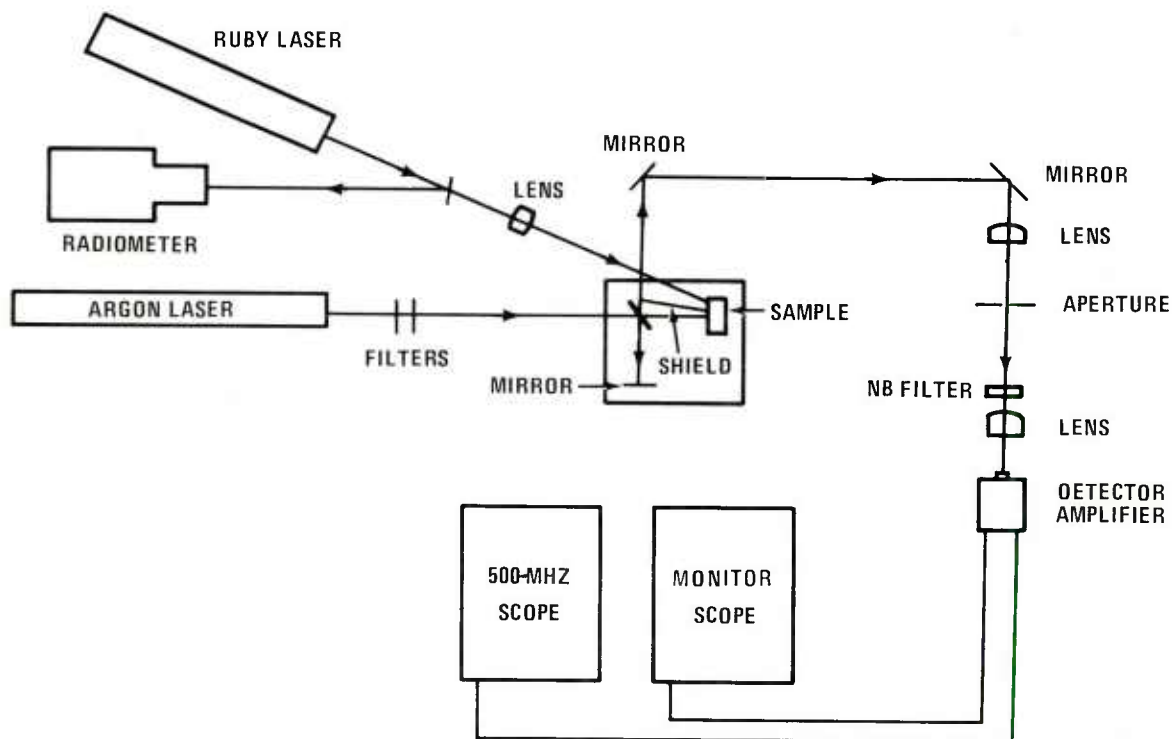
Figure 15. Experimental setup for reflected acoustic wave and flaw-detection experiments.
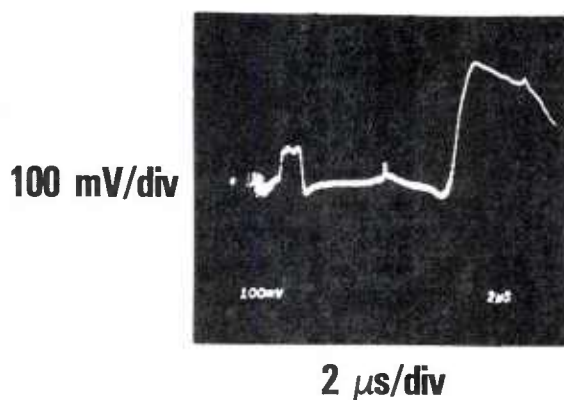

100 mV/div

2 μs/div

Figure 16. Typical acoustic signal observed when generating and readout spots are side by side on one face of sample.

up as a narrow pulse before the pulse reflected from the back face of the sample. The surface wave shown at the beginning of the trace could pose a problem if the flaw in the sample were positioned so that its reflection would show up at the same position as the surface wave.

Experiments aimed at detecting a flaw inside a sample were carried out using the steel sample described above. To simulate a flaw, two 2-mm diameter holes were drilled in the side of the sample, 2.0 cm deep and 1.65 cm from the front face. The distance between the holes was 1 mm. The orientation of the generating spot and the readout spot with respect to the flaw is shown in figure 17. From the position of the holes and the velocity of the bulk wave in steel (about 5.9×10^5 cm/s), the reflection from the holes should be visible about 2.7 μs before the reflection from the back face of the sample. Figure 18(a) shows the signal received by the readout system with this configuration and a generating laser power density of 140 MW/cm². The reflected pulse from the back face is the narrow pulse near the end of the trace,
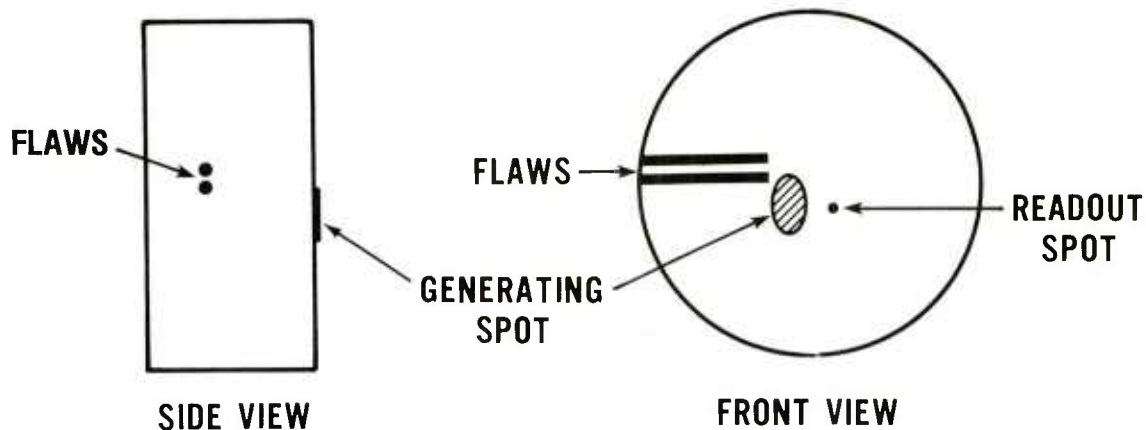
25

Figure 17. Drawing of flawed sample showing orientation of flaw and positions of generating and readout spots.
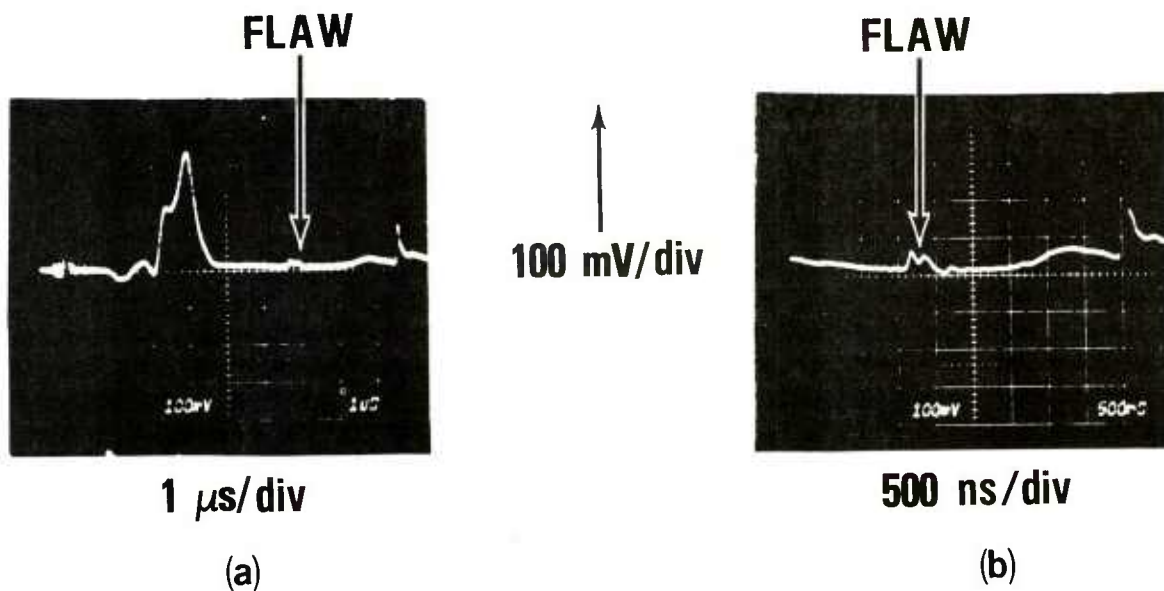

Figure 18. Oscilloscope photographs of acoustic waves observed in flawed sample. Position of flaw is indicated by arrows. Sensitivity is increased by factor of three in part b, and 5-μs delay is added as well.

and the holes are indicated by the double pulse visible about 2.7 μs earlier. By increasing the readout laser power along with the power output of the ruby laser, the system sensitivity was increased three times, as shown in figure 18(b). Reflections from the holes are easily visible in these pictures, and the reflections can easily be distinguished from each other. It is evident that in this case the surface wave did not create a problem for the detection of the interior flaw.

Flaw-detection experiments directed at observing flaws oriented normal to the surface were conducted using a 105-mm artillery shell casing. To accommodate the shell geometry, the readout system had to be modified. The generating laser beam, readout laser beam, flaw, and shell positioning are shown in figure 19. Since the shell surface was not polished and is somewhat diffuse, a focusing lens was needed to collect the readout beam reflection from the shell. In addition, the detection sensitivity was increased by the use of an avalanche photodiode detector. The interfero-

meter was set up with a slight angular misalignment, thereby creating a line or bar interference pattern at the detector. A variable slit and lens were used to aperture this pattern and to focus it onto the detector. With these changes, the sensitivity was essentially the same as when polished surfaces were used. However, the mechanical setup was not as stable as previously. The components of the interferometer, including the sample, could not all be mounted securely to one plate as with the small steel sample experiments, and vibrations in the system caused fringe shifts. Also, due to constraints in mounting the components, the path length in the two legs of the interferometer could not be made nearly the same, thereby creating fringe motion due to laser frequency variation. These problems could be corrected in the following manner. First, the laser stability in both amplitude and frequency could be improved by isolating the laser from reflections from the interferometer. Secondly, a servo-mechanism could slave the mirror position to the fringe position, thereby reducing the variation in the fringe pattern caused by mechanical vibra-
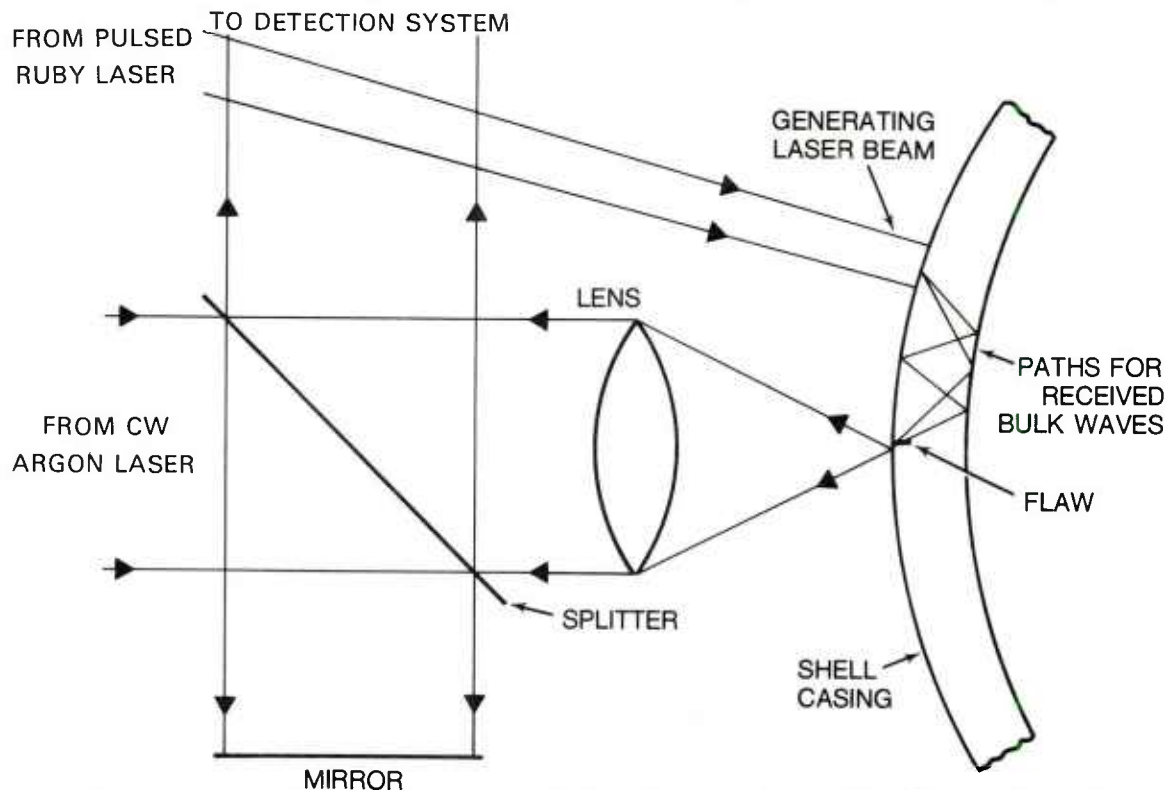

Figure 19. Closeup of positioning of generating and readout spots for flawed 105-mm tank round.

tions. These changes would increase the readout system sensitivity and reproducibility quite markedly. However, due to time constraints, it was decided to use the system with the former defects, even though the combination of the two made it very difficult to get reproducible data, as the position of the fringe pattern prior to the laser pulse was random. The effect of this can be readily seen from figure 4.

Flaws that originate in the 105-mm shells during manufacturing usually run along the length of the shell, penetrating into the shell normal to the shell surface. They occur most frequently on the inside or outside surfaces of the shell casing wall. Flaws with this orientation are inherently more difficult to detect with this system than internally occurring flaws. To simulate the geometry of manufacture-generated flaws, several slots with different dimensions were cut along the length and on the outer surface of the shell. The slot sizes were (a) 4 mm deep, 0.5 mm wide, and 10 mm long; (b) 2 mm deep, 0.5 mm wide, and 10 mm long; and (c) 0.5 mm deep, 0.25 mm wide, and 6 mm long. Flaws (a) and (b) were detectable, but flaw (c) was not, probably due to the instability in the interferometer discussed previously. To detect the flaws, the generating spot was positioned 15 mm from the readout spot, with the flaw being between the two, but as close to the readout spot as possible. The generating spot area was 0.14 cm^2 and the power density at the shell was 170 MW/cm^2. With this configuration the traces in figures 20(a) and (b) were obtained for the 2-mm deep flaw. Figures 20(c) and (d) show similar signals obtained in unflawed regions for the same scale settings. Signals in various unflawed regions showed similar pulse shapes as those shown in figures 20(c) and (d). The signals obtained with the readout spot in an unflawed region are made up of a surface wave that propagates directly from the generating spot to the readout spot combined with bulk wave reflections riding on top of it. The bulk waves produce the narrow spikes that appear on the slower surface

(a)

1 μs/div

(b)

FLAWED

2 μs/div

(c)
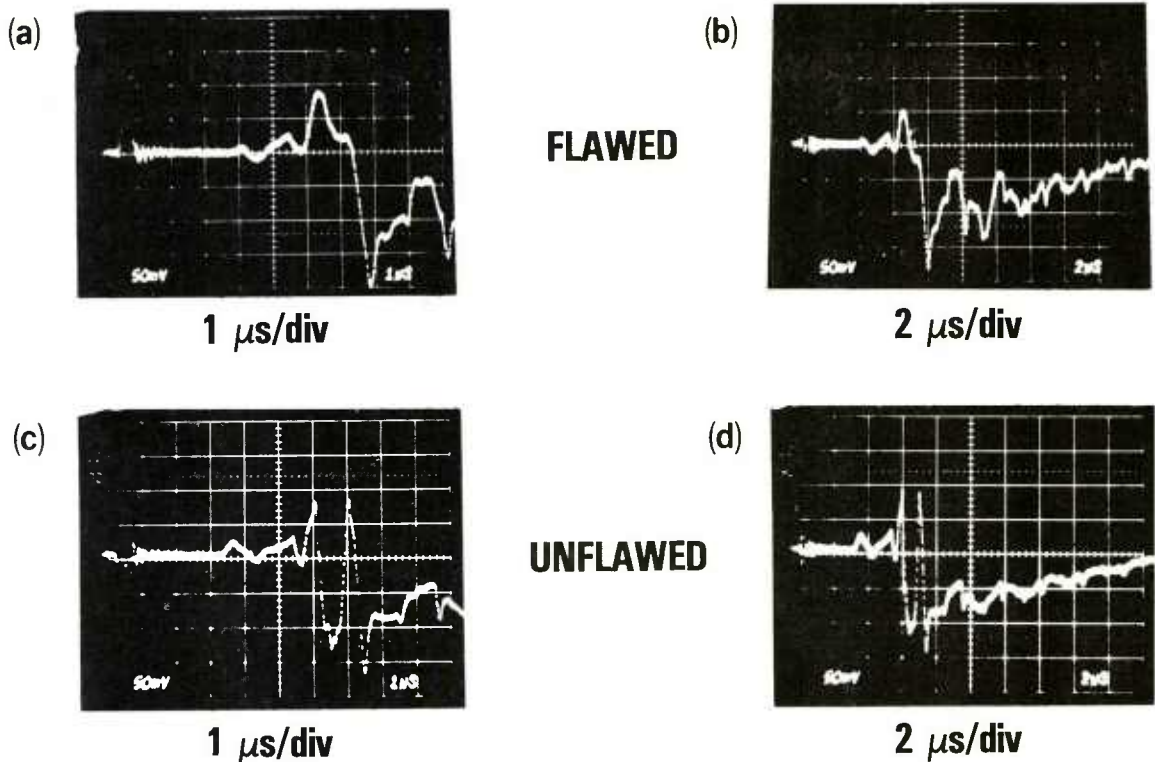
1 μs/div

UNFLAWED

(d)

2 μs/div

Figure 20. Oscilloscope photographs of signal observed for 2-mm deep, 10-mm long by 0.5-mm wide flaw as compared to an unflawed position. The vertical scales are all 50 mV/div.

wave. The traces obtained with the readout spot near the flaw are clearly different than those from an unflawed region. The beginning part of the signal is affected quite noticeably by the flaw, while the later part of the pulse is also different, but not so markedly. This size flaw is easily detectable by comparing the initial part of the pulses, and smaller flaws could be detected once the various acoustic waves in this geometry were identified and the interferometer stabilized. The signals observed with flaw (c) were not significantly different than those observed in an unflawed region. Since flaw (b) was easily detectable, the detection limit for this setup would be smaller than flaw (b) although larger than flaw (c). However, the specific limit is not known since we did not observe the signals for a large number of different sizes of flaws near the detection limit.

5. CONCLUSIONS

We have demonstrated that a high-power laser pulse can generate a longitudinal acoustic wave in a metal sample suitable for use in flaw detection. For a laser power density greater than 50 MW/cm^2 we have detected an acoustic pulse of the same temporal shape as the laser pulse using a BaTiO$_3$ transducer. The acoustic pulse width duplicates the laser pulse width and the amplitude makes the acoustic pulse easily detectable.

We have also shown that under a somewhat idealized situation, the sample under test being ground and polished, a laser interferometer receiver system can easily detect the generated acoustic wave. Signal-to-noise ratios for the detection of the transmitted acoustic wave have approached 50. With an unpolished sample we were able to get an equivalent sensitivity by modifying the readout system.

We have also demonstrated that a side-by-side flaw-detection system, as proposed, can detect flaws in solids, and is a distinct possibility for a practical flaw-detection system. We have shown that with a side-by-side system the acoustic wave reflected from the rear face of the sample is easily detectable. A simulated flaw in the sample, which consisted of two 2-mm diameter holes drilled side by side in the sample, was easily detected, and the holes were easily distinguishable from each other. The practicality of the system for production-line use must still be demonstrated.

Probably the most significant achievement was the detection of a longitudinal flaw in a 105-mm shell casing. We were able to detect a flaw, 2 mm deep by 10 mm long, cut into the shell. This is less than one half the size of a critical flaw in this type of shell casing. A critical flaw is a flaw that has a 50-percent chance of causing the shell to fail during firing.

Improvements in the readout system would allow the detection of even smaller flaws that would give a larger margin of safety. With careful redesign of the readout system, the stability problems discussed in section 4.3 can be solved and overall detection sensitivity can be improved. This redesign should include optically isolating the laser from reflections by the interferometer; mounting the fixed mirror, beam splitter, and focusing lens on one base; designing a diffraction-limited focusing lens; using a variable density optical filter in the reference leg to equalize the power in the reference and test legs; improving the detector electronics; and, finally, using a piezoelectric drive to slave the fixed mirror to maintain constant and optimum phase. The last improvement would have the effect of stabilizing the fringe pattern for low-frequency drift, while not affecting the observation of the (much higher frequency) acoustic signals.

Since a critical flaw is quite large for a 105-mm shell, being 5 mm deep and about 50 mm long, the minimal amount of surface damage done to the shell during the acoustic wave generation process would not create a problem. For other applications the amount of surface damage allowed would have to be determined.

ACKNOWLEDGEMENT

LITERATURE CITED

1. D. A. Giglio, Preliminary Evaluation of a Proposed Laser-Operated Flaw Detection Technique, Harry Diamond Laboratories, HDL-TM-73-32 (December 1973).

2. H. A. Deferrari and F. A. Andrews, Laser Interferometric Technique for Measuring Small-Order Vibration Displacements, J. Acoustic. Soc. Am., *39* (1966), 979-980.

3. S. Sizgoric and A. A. Gundjian, An Optical Homodyne Technique for Measurement of Amplitude and Phase of Subangstrom Ultrasonic Vibrations, Proceedings of IEEE (July 1969), 1313.

4. C. R. Brown, G. R. Brown, and D. H. Niblett, Measurement of Small Strain Amplitudes in Internal Friction Experiments by Means of a Laser Interferometer, J. Physics, E: Scientific Instruments, *5* (1972), 966.

5. G. N. Watson, A Treatise on the Theory of Bessel Functions, Cambridge Press (1952).

6. M. Born and F. Wolf, Principles of Optics, New York, Pergamon Press (1959), 619.

7. J. F. Ready, Effects Due to Absorption of Laser Radiation, J. Appl. Phys., *36*, 2 (February 1965), 462-468.

8. J. C. Bushnell and D. J. McCloskey, Thermoelastic Stress Production in Solids, J. Appl. Phys., *39* (1968), 5541-5546.

9. R. M. White, Generation of Elastic Waves by Transient Surface Heating, J. Appl. Phys., *34* (1963), 3559-3567.

10. L. S. Gournay, Conversion of Electromagnetic to Acoustic Energy by Surface Heating, J. Acoustic. Soc. Am., *40,* 6 (1966), 1322-1330.

11. T. A. Zaker, Stress Waves Generated by Heat Addition in an Elastic Solid, J. Appl. Mech. (March 1965), 143-150.

12. H. S. Carslaw and J. C. Jaeger, Conduction of Heat in Solids, Clarendon Press, Oxford, England (1959).

13. J. F. Ready, Effects of High-Power Laser Radiation, New York, Academic Press (1971).

14. H. Weichel and P. V. Avizonis, Expansion Rates of the Luminous Front of a Laser-Produced Plasma, Appl. Phys. Lett., *9,* 9 (1966), 334-337.

15. D. W. Gregg and S. J. Thomas, Momentum Transfer Produced by Focused Laser Giant Pulses, J. Appl. Phys., *37* (1966), 2787.

16. F. Neuman, Momentum Transfer and Cratering Effects Produced by Giant Laser Pulses, Appl. Phys. Lett., *4* (1964), 167.

17. S. P. Clark, ed., Handbook of Physical Constants, Geological Soc. of America (1966).

18. T. F. Huester and R. H. Bolt, Sonics, New York, John Wiley and Sons Inc. (1955), 106-109.

DISTRIBUTION

COMMANDER
US ARMY ABERDEEN PROVING GROUND
ATTN STEAP-TL, TECH LIB
ABERDEEN PROVING GROUND, MD 21005

COMMANDER
US ARMY ELECTRONICS PROVING GROUND
ATTN STEEP-PA-I, TECH INFO CENTER
FORT HUACHUCA, AZ 85613

COMMANDER
US ARMY YUMA PROVING GROUND
ATTN STEYP-MSA, TECHNICAL LIB
YUMA, AZ 85364

CHIEF OF NAVAL RESEARCH
DEPT OF THE NAVY
ATTN TECHNICAL LIBRARY
ARLINGTON, VA 22217

SUPERINTENDANT
NAVAL POSTGRADUATE SCHOOL
ATTN LIBRARY, CODE 2124
MONTEREY, CA 93940

DIRECTOR
NAVAL RESEARCH LABORATORY
ATTN 2600, TECHNICAL INFO DIV
WASHINGTON, DC 20375

COMMANDER
NAVAL SEA SYSTEMS COMMAND HQ
DEPT OF THE NAVY
ATTN NSEA-09G32, TECH LIB
WASHINGTON, DC 20362

COMMANDER
NAVAL SHIP R&D CENTER
ATTN LIBRARY DIV
BETHESDA, MD 20034

COMMANDER
NAVAL SURFACE WEAPONS CENTER
ATTN DX-21, LIBRARY DIV
DAHLGREN, VA 22448

COMMANDER
NAVAL SURFACE WEAPONS CENTER
ATTN WX-40 TECHNICAL LIB
WHITE OAK, MD 20910

COMMANDER
NAVAL WEAPONS CENTER
ATTN 06, TEST & EVALUATION DIV
CHINA LAKE, CA 93555

COMMANDER
HQ AIR FORCE SYSTEMS COMMAND
ANDREWS AFB
ATTN TECHNICAL LIBRARY
WASHINGTON, DC 20334

OREGON STATE UNIV. DEPT OF ME
ATTN CLARENCE CALDER
CORVALLIS, OR 97331

GENERAL DYNAMICS
ATTN P. R. DE TONNANCOUR (LIBRARIAN)
P.O. BOX 748
FORT WORTH, TX 76101

BETHLEHEM STEEL CORP
ATTN RICHARD KLINMAN
BUILDING A RM C128
BETHLEHEM, PA 18016

TENN. TECH. UNIVERSITY
ATTN DR. J. RICHARD HOUGHTON
COLLEGE OF ENGINEERING
COOKEVILLE, TN 38501

JOHNS HOPKINS UNIVERSITY
ATTN DR. ROBERT GREEN
MATERIAL SCIENCES & ENGINEERING
BALTIMORE, MD 21218

UNIVERSITY OF HULL
ATTN DR. R. J. DEWHURST
DEPT OF APPL. PHYSICS
HULL, HU6 7RX
ENGLAND

UNVERSITY OF HOUSTON
ATTN DR. C. GERALD GARDNER
PROF. OF ENG. SCIENCE
CULLEN COLLEGE OF ENG.
HOUSTON, TX 77004

US ARMY ELECTRONICS RESEARCH
 & DEVELOPMENT
ATTN TECHNICAL DIRECTOR, DRDEL-CT
ATTN D. GIGLIO, CM/CCM

HARRY DIAMOND LABORATORIES
 ATTN 00100 COMMANDER/TECH DIR/TSO
 ATTN CHIEF, DIV 10000
 ATTN CHIEF, DIV 20000
 ATTN CHIEF, DIV 30000
 ATTN CHIEF, DIV 40000
 ATTN RECORD COPY, 81200
 ATTN HDL LIBRARY, 81100 (3 COPIES)
 ATTN HDL LIBRARY, 81100 (WOODBRIDGE)
 ATTN TECHNICAL REPORTS BRANCH, 81300
 ATTN CHAIRMAN, EDITORIAL COMMITTEE
 ATTN J. NEMARICH, 13300
 ATTN Z. SZTANKAY, 13300
 ATTN CHIEF, 13000
 ATTN R. JOHNSON, 15200
 ATTN N. KARAYIANIS, 13200
 ATTN R. N. GOTTRON, 13400
 ATTN CHIEF, 95000
 ATTN R. WELLMAN, 13300 (20 COPIES)

ADMINISTRATOR
DEFENSE DOCUMENTATION CENTER
ATTN DDC-TCA (12 COPIES)
CAMERON STATION, BUILDING 5
ALEXANDRIA, VA 22314

COMMANDER
US ARMY RSCH & STD GP (EUR)
ATTN LTC JAMES M. KENNEDY, JR.
     CHIEF, PHYSICS & MATH BRANCH
FPO NEW YORK 09510

COMMANDER
US ARMY MATERIEL DEVELOPMENT &
 READINESS COMMAND
ATTN DRXAM-TL, HQ TECH LIBRARY
5001 EISENHOWER AVENUE
ALEXANDRIA, VA 22333

COMMANDER
US ARMY ARMAMENT MATERIEL
 READINESS COMMAND
ATTN DRSAR-LEP-L, TECHNICAL LIBRARY
ATTN DRSAR-ASF, FUZE & MUN
     SUPPORT DIV
ROCK ISLAND, IL 61299

COMMANDER
US ARMY MISSILE & MUNITIONS
 CENTER & SCHOOL
ATTN ATSK-CTD-F
REDSTONE ARSENAL, AL 35809

DIRECTOR
US ARMY MATERIEL SYSTEMS ANALYSIS ACTIVITY
ATTN DRXSY-MP
ABERDEEN PROVING GROUND, MD 21005

DIRECTOR
US ARMY BALLISTIC RESEARCH LABORATORY
ATTN DRDAR-TSB-S (STINFO)
ABERDEEN PROVING GROUND, MD 21005

TELEDYNE BROWN ENGINEERING
CUMMINGS RESEARCH PARK
ATTN DR. MELVIN L. PRICE, MS-44
HUNTSVILLE, AL 35807

ENGINEERING SOCIETIES LIBRARY
345 EAST 47TH STREET
ATTN ACQUISITIONS DEPARTMENT
NEW YORK, NY 10017

US ARMY ELECTRONICS TECHNOLOGY
 & DEVICES LABORATORY
ATTN DELET-DD
FORT MONMOUTH, NJ 07703

BROOKHAVEN NATIONAL LABORATORY
ASSOCIATED UNIVERSITIES, INC.
ATTN MECHANICAL ENGINEERING
ATTN PHYSICS DEPT
UPTON, LONG ISLAND, NY 11973

DEPARTMENT OF COMMERCE
NATIONAL BUREAU OF STANDARDS
ATTN LIBRARY
ATTN GEORGE BIRNBAUM
WASHINGTON, DC 20234

DIRECTOR
DEFENSE COMMUNICATIONS AGENCY
ATTN TECH LIBRARY
WASHINGTON, DC 20305

DIRECTOR
DEFENSE COMMUNICATIONS ENGINEERING CENTER
ATTN TECHNICAL LIBRARY
1860 WIEHLE AVE
RESTON, VA 22090

DIRECTOR
DEFENSE NUCLEAR AGENCY
ATTN STSP, SHOCK PHYSICS DIRECTORATE
WASHINGTON, DC 20305

UNDER SECRETARY OF DEFENSE
 FOR RESEARCH & ENGINEERING
ATTN DEP DIR (TEST & EVALUATION)
WASHINGTON, DC 20301

OFFICE OF THE DEPUTY CHIEF OF STAFF
 FOR RESEARCH, DEVELOPMENT,
 & ACQUISITION
ATTN DAMA-ARZ-A, CHIEF SCIENTIST,
     DA & DIRECTOR OF ARMY RESEARCH,
     DR. M. E. LASSER
ATTN DAMA-CSM, MUNITIONS DIV
DEPARTMENT OF THE ARMY
WASHINGTON, DC 20310

COMMANDER
US ARMY ARMAMENT RESEARCH AND
 DEVELOPMENT COMMAND
ATTN DRDAR-SEM, MATERIEL DEV EVAL
ATTN DRDAR-QA, PRODUCT ASSURANCE DIV
ATTN DRDAR-TS, TECHNICAL SUPPORT DIV
ATTN DRDAR-QAR-I, MARK WEINBERG
ATTN DRDAR-LCA, PAUL KISATSKY
ATTN DRDAR-QAN, P. G. OLIVIERI
DOVER, NJ 07801

COMMANDER
ARRCOM
ATTN DRSAR-MAD-C,
     AMMUNITION MAINTENANCE ENGR BR
DOVER, NJ 07801

COMMANDER
US ARMY ARMOR CENTER
ATTN TECHNICAL LABORATORY
FORT KNOX, KY 40121

COMMANDER
US ARMY COMMUNICATIONS RESEARCH AND
 DEVELOPMENT COMMAND
ATTN DRDCO-PT, PRODUCT ASSURANCE
      & TEST DIR
ATTN DRDCO-PE, PRODUCTION ENGR
      SUPPORT DIR
FT. MONMOUTH, NJ 07703

COMMANDER
US ARMY COMMUNICATIONS & ELECTRONICS
 MATERIEL READINESS COMMAND
ATTN SELEM-QA, QUALITY ASSURANCE OFC
FT. MONMOUTH, NJ 07703

DIRECTOR
ELECTRONIC WARFARE LABORATORY
ATTN DELEW-PE, PRODUCTION ENGR OFC
FT. MONMOUTH, NJ 07703

COMMANDER
US ARMY FOREIGN SCIENCE
 & TECHNOLOGY CENTER
ATTN DRXST-IS3, LIBRARY
FEDERAL OFFICE BLDG
220 7TH STREET, NE
CHARLOTTESVILLE, VA 22901

COMMANDER
US ARMY MATERIALS & MECHANICS
 RESEARCH CENTER
ATTN DRXMR-PL, TECHNICAL LIBRARY
ATTN DRXMR-T, MECHANICS RES LAB
ATTN DRXMR-X, DR. F. S. WRIGHT
ATTN DRXMR-MI, GEORGE A DARCY
WATERTOWN, MA 02172

COMMANDER
US ARMY MISSILE MATERIEL
 READINESS COMMAND
ATTN DRSMI-Q, DIR FOR PRODUCT
      ASSURANCE
REDSTONE ARSENAL, AL 35809

COMMANDER
US ARMY MISSILE RES & DEV COMMAND
ATTN DRDMI-ET, TEST & EVALUATION DIR
ATTN DRDMI-Q, PRODUCT ASSURANCE DIR
ATTN DRDMI-E, HORACE LOWERS
REDSTONE ARSENAL, AL 35809

COMMANDER
US ARMY NATICK RES & DEV COMMAND
US ARMY NATICK DEVELOPMENT CENTER
ATTN DRDNA-T, TECHNICAL LIBRARY
NATICK, MA 01760

DIRECTOR
NIGHT VISION & ELECTRO-OPTICS
 LABORATORY
ATTN DELNV-L LASER DIV
FORT BELVOIR, VA 22060

DIRECTOR
US ARMY RESEARCH AND TECHNOLOGY
 LABORATORIES
AMES RESEARCH CENTER
ATTN SAUDL-AS, FRED IMMEN
MOFFETT FIELD, CA 94035

DIRECTOR
US ARMY SIGNALS WARFARE LABORATORY
ATTN DELSW-TE, TEST & EVAL OFC
VINT HILL FARMS STATION
WARRENTON, VA 22186

COMMANDER
US ARMY TANK-AUTOMOTIVE MATERIEL
 READINESS COMMAND
DEPT OF THE ARMY
ATTN DRSTA-F,
      DIR FOR MATERIEL MANAGEMENT
WARREN, MI 48090

COMMANDER
US ARMY TANK-AUTOMOTIVE RES
 & DEV COMMAND
DEPT OF THE ARMY
ATTN DRCPM-CVT, ARMORED COMBAT
      VEHICLE TECHNOLOGY
WARREN, MI 48090

COMMANDER
HQ, US ARMY TEST & EVALUATION COMMAND
ATTN DRSTE-CT, COMBAT SUPPORT SYS
      MATERIEL TEST DIR
ABERDEEN PROVING GROUND, MD 21005

COMMANDER
WHITE SANDS MISSILE RANGE
DEPT OF THE ARMY
ATTN STEWS-TE, ARMY MAT TEST
      & EVALUATION DIR
WHITE SANDS MISSILE RANGE, NM 88002

COMMANDER
EDGEWOOD ARSENAL
ATTN SAREA-TS, TECH LIB
EDGEWOOD ARSENAL, MD 21010

COMMANDER
ROCK ISLAND ARSENAL
ATTN SARRI-ENE, ENGR & TEST DIV
ROCK ISLAND, IL 61201